

University of Dundee

Multimic profiling of breast cancer cells uncovers stress MAPK-associated sensitivity to AKT degradation

Erickson, Emily C.; You, Inchul; Perry, Grace; Dugourd, Aurelien; Donovan, Katherine A.; Crafter, Claire

Published in:
Science Signaling

DOI:
[10.1126/scisignal.adf2670](https://doi.org/10.1126/scisignal.adf2670)

Publication date:
2024

Licence:
CC BY

Document Version
Peer reviewed version

[Link to publication in Discovery Research Portal](#)

Citation for published version (APA):

Erickson, E. C., You, I., Perry, G., Dugourd, A., Donovan, K. A., Crafter, C., Johannes, J. W., Williamson, S., Moss, J. I., Ros, S., Ziegler, R. E., Barry, S. T., Fischer, E. S., Gray, N. S., Madsen, R. R., & Toker, A. (2024). Multimic profiling of breast cancer cells uncovers stress MAPK-associated sensitivity to AKT degradation. *Science Signaling*, 17(825). <https://doi.org/10.1126/scisignal.adf2670>

General rights

Copyright and moral rights for the publications made accessible in Discovery Research Portal are retained by the authors and/or other copyright owners and it is a condition of accessing publications that users recognise and abide by the legal requirements associated with these rights.

Take down policy

If you believe that this document breaches copyright please contact us providing details, and we will remove access to the work immediately and investigate your claim.

1 **Now published under a CC BY-4.0 license:**

2 <https://www.science.org/doi/10.1126/scisignal.adf2670>

3
4
5 **Multomic profiling of breast cancer cells uncovers**
6 **stress MAPK-associated sensitivity to AKT degradation**
7

8
9 Emily C. Erickson^{1,5,10}, Inchul You^{2,10}, Grace Perry¹, Aurelien Dugourd³, Katherine A.
10 Donovan^{4,5}, Claire Crafter⁶, Jeffrey W. Johannes⁷, Stuart Williamson⁶, Jennifer I. Moss⁶, Susana
11 Ros⁶, Robert E. Ziegler⁷, Simon T. Barry⁶, Eric S. Fischer^{4,5}, Nathanael S. Gray², Ralitsa R.
12 Madsen^{8,9*}, Alex Toker^{1*}

13 ¹Department of Pathology, Medicine and Cancer Center, Beth Israel Deaconess Medical
14 Center, Harvard Medical School, Boston, MA 02215, USA.

15 ²Department of Chemical and Systems Biology, Stanford University, Stanford, CA 94305, USA

16 ³Faculty of Medicine, and Heidelberg University Hospital, Institute for Computational
17 Biomedicine, Heidelberg University, Heidelberg 69120, Germany

18 ⁴Department of Cancer Biology, Dana-Farber Cancer Institute, Boston, MA 02215, USA

19 ⁵Department of Biological Chemistry and Molecular Pharmacology, Harvard Medical School,
20 Boston, MA 02215, USA

21 ⁶Research and Early Development, Oncology R&D, AstraZeneca, Cambridge CB2 0AA, UK

22 ⁷Research and Early Development, Oncology R&D, AstraZeneca, Waltham, MA 02451, USA

23 ⁸University College London Cancer Institute, Paul O'Gorman Building, University College
24 London, London WC1E 6BT, UK

25 ⁹ Current: MRC-Protein Phosphorylation and Ubiquitylation Unit, School of Life Sciences,
26 University of Dundee, Dundee DD1 5EH, UK

27 ¹⁰ These authors contributed equally to this work

28 *Corresponding: atoker@bidmc.harvard.edu, madsen001@dundee.ac.uk

29
30

'This research was funded in whole, or in part by the Wellcome Trust [Grant number 220464/Z/20/Z]. For the purpose of open access, the author has applied a CC BY public copyright licence to any Author Accepted Manuscript version arising from this submission.'

31 **Abstract**

32 More than 50% of human tumors display hyperactivation of the serine/threonine kinase AKT.
33 Despite evidence of clinical efficacy, the therapeutic window of the current generation of AKT
34 inhibitors could be improved. Here, we report the development of a second-generation AKT
35 degrader, INY-05-040, which outperformed catalytic AKT inhibition with respect to cellular
36 suppression of AKT-dependent phenotypes in breast cancer cell lines. A growth inhibition screen
37 with 288 cancer cell lines confirmed that INY-05-040 had a substantially higher potency than our
38 first-generation AKT degrader (INY-03-041), with both compounds outperforming catalytic AKT
39 inhibition by GDC-0068. Using multiomic profiling and causal network integration in breast
40 cancer cells, we demonstrated that the enhanced efficacy of INY-05-040 was associated with
41 sustained suppression of AKT signaling, which was followed by induction of the stress mitogen
42 activated protein kinase (MAPK) c-Jun N-terminal kinase (JNK). Further integration of growth
43 inhibition assays with publicly available transcriptomic, proteomic, and reverse phase protein
44 array (RPPA) measurements established low basal JNK signaling as a biomarker for breast
45 cancer sensitivity to AKT degradation. Together, our study presents a framework for mapping
46 the network-wide signaling effects of therapeutically relevant compounds and identifies INY-05-
47 040 as a potent pharmacological suppressor of AKT signaling.

48

49

50 **Introduction**

51 The phosphoinositide 3-kinase (PI3K)/AKT network has a fundamental role in the
52 integration of extracellular growth stimuli to regulate cell metabolism, migration, proliferation,
53 and survival¹. Aberrant activation of this network is widespread in human cancers, particularly
54 those of the female reproductive system². Numerous therapies targeting PI3K/AKT pathway
55 components have been developed and evaluated for their potential as cancer therapeutics, and
56 some have been clinically approved, including the PI3K α -specific inhibitor alpelisib (PIQRAY®)
57 for ER⁺/HER2⁻ breast cancer³. Because of its central role in mediating PI3K signaling and
58 frequent hyperactivation across cancer types, the serine/threonine protein kinase AKT has
59 become an attractive therapeutic target⁴⁻⁶. Several drugs targeting AKT have been developed
60 and evaluated in clinical trials, including ATP-competitive, allosteric, and covalent pan-AKT
61 inhibitors⁷⁻¹¹. These inhibitors have yet to be approved for the treatment of cancer. Despite
62 promising outcomes in some phase II and ongoing phase III clinical studies¹², there is room to
63 improve the therapeutic window of available AKT-targeting compounds. Moreover, conventional
64 AKT inhibitors are largely cytostatic, not cytotoxic, thus failing to eradicate cancer cells as
65 monotherapies. Consequently, there is an unmet need to identify more potent AKT-targeting
66 drugs, in addition to uncovering cellular mechanisms that contribute to the efficacy of AKT
67 inhibition.

68 Targeted protein degradation using small molecule degraders, also called PROTACs
69 (proteolysis targeting chimeras), has emerged as a therapeutic modality and as a tool for the
70 chemical depletion of proteins of interest¹³⁻¹⁶. In many cases, PROTACs display increased
71 selectivity over the inhibitors from which they are designed, which presents advantages in
72 limiting off-target toxicities¹⁷. Targeted protein degradation can also be used as a tool to
73 understand network rewiring dynamics following near-complete and relatively acute depletion of

74 the protein of interest. Potent and selective AKT-targeting PROTACs have been developed, with
75 improved selectivity and potency over parental AKT inhibitors¹⁸⁻²¹.

76 Here, we report the development of a second-generation AKT degrader, INY-05-040,
77 which selectively and rapidly (<5 h) degrades all three AKT isoforms and inhibits downstream
78 signaling and cell proliferation in 288 cancer cell lines. Using a multiomics approach, combined
79 with computational network modeling and experimental validation, we uncovered several
80 degrader-selective cellular phenotypes in breast cancer cells, including potent activation of the
81 stress mitogen activated protein kinase (MAPK) c-Jun N-terminal kinase 1 (JNK1). Additional
82 breast cancer cell line analyses revealed that a signature of baseline JNK1 activation predicts
83 lower sensitivity to AKT degradation, suggesting a potential biomarker for therapeutic
84 stratification.

85 **Results**

86 **INY-05-040 is an improved AKT degrader**

87 We previously reported the development of an AKT-targeting degrader INY-03-041, a
88 heterobifunctional degrader consisting of the catalytic AKT inhibitor GDC-0068 chemically linked
89 to the Cereblon (CRBN) recruiter lenalidomide⁷. Despite the potency and selectivity of INY-03-
90 041, this degrader exhibited relatively slow (12 h) cellular degradation kinetics for all three AKT
91 isoforms²⁰. We therefore developed an improved AKT degrader, INY-05-040, consisting of
92 GDC-0068 chemically conjugated to a Von Hippel-Lindau (VHL) ligand with a ten-hydrocarbon
93 linker (**Fig. 1A**). To generate the matched negative control compound INY-05-040-Neg (**Fig.**
94 **1A**), we incorporated a diastereoisomer of the VHL ligand that substantially loses activity
95 towards VHL²². The biochemical selectivity of INY-050-040 was comparable to GDC-0068
96 across a panel of 468 kinases (**Fig. S1A**). A proteomic screen of the MOLT4 T lymphoblast cell
97 line, which expresses all three AKT isoforms, confirmed pan-AKT downregulation following 4-h
98 treatment with 250 nM INY-05-040 (**Fig. S1B**).

99 All subsequent evaluation of INY-05-040 was performed as part of a screen of human
100 breast cancer cell lines, due to the high prevalence of PI3K/AKT pathway activation. Exposure
101 of the estrogen receptor-positive (ER+) and *PIK3CA*^{H1047R}-mutant T47D cell line to increasing
102 doses of INY-050-040 for 5 h (**Fig.1B**) or over a time course using a dose of 100 nM (**Fig.1C**)
103 revealed an improved dose- and time-dependent reduction in total AKT levels compared to the
104 first-generation degrader, INY-03-041. This was mirrored by suppression of downstream
105 PRAS40 (Thr²⁴⁶) and S6 (Ser²⁴⁰/Ser²⁴⁴) phosphorylation (**Fig.1B, 1C**). INY-05-040 also
106 outperformed GDC-0068 in T47D cells treated for 24 h, with >500 nM of GDC-0068 required to
107 achieve comparable signaling suppression to that achieved with 50-100 nM INY-05-040
108 (**Fig.1D**). Because GDC-0068 is also a component of the negative control compound, INY-05-
109 040-Neg, the latter suppressed signaling at higher concentrations (**Fig. S1C**), as expected.
110 Unlike non-covalent, catalytic inhibition of AKT with GDC-0068, INY-05-040 treatment of T47D
111 cells resulted in sustained AKT reduction and suppression of downstream signaling for at least
112 72 h following compound washout (**Fig. 1E**). Consistent with proteasome-dependent
113 degradation, pharmacological abrogation of proteasomal function or neddylation prevented AKT
114 degradation by INY-05-040 (**Fig. S1F**). We replicated these experiments in a screen of the
115 *PTEN*-deficient triple-negative breast cancer (TNBC) MDA-MB-468 cell line (**Fig. S1D, S1E,**
116 **S1F, S1G**), suggesting that the favorable cellular properties of INY-05-040 are generalizable
117 across breast cancer cell lineages. Cells exposed to INY-05-040 also exhibited reduced levels
118 of total ribosomal S6 protein, which was observed within the first 24 h of treatment as well as
119 after compound wash-out (**Fig. 1C, 1D, 1E, S1E**). Consistent with rapid and long-term
120 downregulation of AKT signaling, our second-generation AKT degrader INY-05-040 caused
121 suppression of cell growth across four different breast cancer cell lines, at doses that were
122 below those required for an equivalent response with catalytic inhibitors and lower or similar
123 with respect to allosteric AKT inhibitors (**Fig. S1H, S1I**).

124 Furthermore, we tested the pharmacokinetic and pharmacodynamic properties of AKT
125 degraders in vivo (Tables S1-S4). After 4 days of treatment in a BT-474C breast cancer
126 xenograft model, both first- (INY-03-041) and second-generation (INY-05-040) degraders
127 caused potent reduction in pan-AKT levels, which was accompanied by decreased
128 phosphorylation of PRAS40 (Thr²⁴⁶) and pS6 (Ser^{240/244}) (**Fig. 1F**). Likely due to incomplete AKT
129 degradation in vivo, the observed suppression of downstream signaling was similar to that
130 observed with GDC-0068. Together, these results show that INY-05-040 is a potent AKT
131 degrader and inhibitor of downstream signaling output, outperforming both our first-generation
132 AKT degrader and GDC-0068.

133 **Multi-omic profiling reveals AKT degrader-selective responses**

134 To identify mechanisms unique to AKT degradation relative to catalytic inhibition, we
135 performed mRNA sequencing (RNAseq) analysis of T47D breast cancer cells that were treated
136 for 5 or 10 h and grown in nutrient- and growth factor-replete cell culture media. To limit the
137 confounding effect of differential potency, we determined the doses of INY-05-040 (100 nM) and
138 GDC-0068 (500 nM) that resulted in comparable suppression of downstream signaling at these
139 time points (**Fig. S2**).

140 Consistent with a shared target, the transcriptomes of GDC-0068- and INY-05-040-treated
141 cells clustered closely together, separate from DMSO- and INY-05-040-Neg-treated controls,
142 according to an unsupervised principal component analysis (PCA) (**Fig. 2A**). In agreement with
143 the slower onset of AKT degradation, 5-h treatment with INY-05-040 resulted in differential
144 abundance of only 194 transcripts (100 decreased, 94 increased; absolute fold-change ≥ 1.3),
145 compared to 511 transcripts (249 decreased, 262 increased) with GDC-0068 during the same
146 period (**Fig. 2B**). By contrast, after 10 h, INY-05-040 caused differential abundance of 1394
147 transcripts (626 decreased, 768 increased; absolute fold-change ≥ 1.3), whereas the extent of
148 GDC-0068-induced transcriptional changes remained stable at 543 transcripts (243 decreased;

149 300 increased) (**Fig. 2B**). Across all differentially expressed transcripts after 10-h treatment,
150 more than 700 were unique to INY-05-040, compared to less than 100 unique changes for
151 GDC-0068 (**Fig. S3A, S3B**). No differential abundance was observed in response to treatment
152 with the control compound INY-05-040-Neg (**Fig. 2B**).

153 We next conducted gene set enrichment analysis (GSEA) using the HALLMARK gene
154 signature collection provided by the Broad Institute Molecular Signature Database (MSigDB)²³.
155 At 10 h, both INY-05-040 and GDC-0068 triggered a transcriptional footprint consistent with
156 suppression of the cell cycle, glycolysis, oxidative phosphorylation, mTORC1 and the unfolded
157 protein response (UPR) (**Fig. 2C, 2D**). Although 5-h treatment with GDC-0068 resulted in a
158 larger number of distinct gene signatures with positive enrichment scores, most of these no
159 longer reached statistical significance after 10 h (**Fig. 2D**), suggesting emerging adaptation to
160 catalytic AKT inhibition. After 10-h treatment, positively enriched gene signatures were largely
161 shared between degrader and catalytic inhibitor, but the underlying gene expression shifts were
162 often more robust following AKT degradation, as evidenced by higher statistical significance
163 despite equivalent sample size (**Fig. 2C, 2D**). Examples include gene signatures related to
164 apoptosis, inflammatory signaling (including TNF α and NF κ B) and the mitotic spindle (**Fig. 2C,**
165 **2D**).

166 We next used DoRothEA, a transcriptional footprint-based method featuring a curated
167 gene regulatory network²⁴, to predict differences in transcription factor regulation between INY-
168 05-040 and GDC-0068 at 10 h. Overall, transcription factor activity predictions were highly
169 concordant between the two compounds, with two notable exceptions. The lipid and sterol
170 metabolism-regulating transcription factors, SREBP1 and SREBP2, were predicted as strongly
171 inhibited upon catalytic AKT inhibition but not AKT degradation (**Fig. 2E**). A correlation analysis
172 across the previously generated HALLMARK gene signature enrichments revealed a similar
173 discordance with respect to cholesterol homeostasis and androgen response signatures (**Fig.**

174 **2F**). Of note, these two signatures shared four transcripts related to lipid and cholesterol
175 synthesis: *SCD*, *IDI1*, *HMGCR*, and *HMGCS1*. Both *HMGCR* and *HMGCS1* belong to the list of
176 SREBP1 and SREBP2 targets whose mRNA levels were increased upon 10-h treatment with
177 INY-05-040 but not GDC-0068 (**Fig. S3C**).

178 These findings were further supported by results from precision nuclear run-on
179 sequencing (PRO-seq) analysis performed on T47D cells exposed to INY-05-040 or GDC-0068
180 for 5 h. PRO-seq analysis allows mapping of RNA polymerase active sites with base-pair
181 resolution²⁵, and changes in the expression of a transcript reflect immediate differences in active
182 transcription, unlike RNAseq analysis, which captures steady-state mRNA levels. Similar to the
183 bulk transcriptomes, PRO-seq datasets from degrader- and GDC-0068-treated samples
184 clustered together and away from DMSO-treated controls by PCA (**Fig. S3D**). A substantially
185 higher number of genes were differentially transcribed in response to AKT degradation (**Fig.**
186 **S3E, S3F**), with further functional enrichment analyses supporting transcriptional regulation of
187 SREBP1/2 and cholesterol homeostasis as defining differences between AKT degradation
188 versus catalytic inhibition (**Fig. 2G, 2H**). Such activation of SREBP1 and SREBP2, despite
189 potent AKT/mTORC1 inhibition, would be consistent with a phenotype of cholesterol depletion²⁶.

190 Given evidence for altered metabolic homeostasis, we next assessed the metabolic profile
191 of T47D cells treated with INY-05-040 and GDC-0068. For comparison, we also included an
192 allosteric (MK-2206) and a second catalytic (AZD 5363) inhibitor. Treatments were performed
193 for 24 h to allow capture of robust and persistent changes while minimizing the signaling
194 rebound seen with GDC-0068 upon continuous treatment (**Fig. S4**). LC-MS-based
195 metabolomics analysis showed that AKT degradation caused the largest number of differentially
196 abundant metabolites (**Fig. 2I**). Many metabolite changes were shared across AKT-targeting
197 compounds, especially MK-2206 and AZD 5363. Several nucleosides and their phosphorylated
198 derivatives had increased in abundance, including inosine, guanosine, IMP, GMP, AMP and

199 CMP. Metabolite changes unique to treatment with INY-05-040 included intermediates of the
200 hexosamine biosynthesis pathway, the pentose phosphate pathway, glycolysis, the tricarboxylic
201 acid cycle, glutathione and cholesterol metabolism (**Fig. 2I**). Only AKT degradation caused
202 increased levels of methylmalonic acid (MMA), which is a potent inhibitor of the rate-limiting
203 cholesterol biosynthesis enzyme HMGCR²⁷. MMA accumulates if vitamin B12 levels are too low
204 relative to the catabolism of branched chain amino acids and odd chain fatty acids²⁸. Together,
205 this multiomic approach supports a widespread perturbation of cellular homeostasis in breast
206 cancer cells treated with INY-05-040, with distinct responses to AKT degradation pertaining to
207 cholesterol homeostasis.

208 **COSMOS analysis identifies altered stress MAPK signaling downstream of AKT** 209 **degradation**

210 We next reasoned that an integrated, transomic integration of the previous datasets may
211 enable us to generate testable mechanistic hypotheses regarding previously unknown signaling
212 changes downstream of AKT degradation. We applied the COSMOS (causal oriented search of
213 multi-omic space) network analysis approach²⁹ to integrate transcriptomic and metabolomic
214 datasets following treatment with the AKT degrader INY-05-040 or GDC-0068 for 10 h and 24 h,
215 respectively (**Fig. 3A**). Briefly, COSMOS relies on an extensive prior knowledge network (PKN)
216 of signaling pathways, transcriptional regulation and metabolic reactions, in combination with an
217 integer linear programming (ILP) optimization strategy to identify the smallest coherent
218 subnetwork causally connecting as many deregulated transcription factors and metabolites in
219 the input data as possible^{29,30}. Input data to COSMOS consisted of the background
220 transcriptome of T47D cells, in addition to treatment-specific DoRothEA-derived transcription
221 factor activity predictions and differentially abundant metabolites. The resulting networks enable
222 identification of top degree signaling nodes or “hubs”, which are essential for holding a network
223 together due to their high number of connections³¹. Replicate COSMOS runs identified MAPK1

224 (also known as ERK2) and/or MAPK3 (also known as ERK1) as top degree nodes in both INY-
225 05-040 and GDC-0068 networks (**Fig. 3B, 3C; S5A, S5B**), consistent with the known
226 compensatory RAS/MAPK signaling activation that follows potent PI3K/AKT pathway
227 inhibition^{32,33}. Focusing on unique differences, we noted that the stress MAPKs, MAPK8 (also
228 known as JNK1) and MAPK14 (also known as p38 α), were among the top degree nodes in the
229 INY-05-040-specific networks (**Fig. 3B**). MAPK14 was identified as a top degree node in 10 out
230 of 11 COSMOS runs with INY-05-040 input data but was never a top degree node in any of the
231 eight COSMOS runs performed with GDC-0068 input data (**Fig. 3B, 3C**). In two out of eight
232 GDC-0068-specific networks, MAPK14 was not part of the final network; in the remaining six, it
233 had a maximum of two connections per network, suggesting a minor role for this kinase in the
234 cellular response to GDC-0068.

235 To corroborate these findings, we next retrieved all MSigDb curated gene sets (C2
236 collection) featuring transcriptional changes downstream of JNK/p38 perturbation and
237 performed GSEA using the RNAseq dataset. Three gene signatures related to TNF α signaling
238 were positively and significantly enriched in INY-05-040-treated T47D cells after 10 h, with two
239 of the signatures representing transcriptional changes that are either completely or partially
240 dependent on p38 (**Fig. 3D**). These signatures originated from a study examining the response
241 of lung cancer cells to TNF α in the presence or absence of the pan-p38 inhibitor LY479754³⁴.
242 Only one of the two p38-dependent signatures were significantly enriched for with a positive
243 score in GDC-0068-treated cells; however, neither the significance nor the magnitude of
244 enrichment were as strong as that observed in INY-05-040-treated cells (**Fig. 3D**). This is also
245 consistent with a much weaker enrichment of the hallmark gene signature
246 “TNFA_signaling_via_NF κ B” in response to 10-h treatment with GDC-0068 compared to INY-
247 05-40 (**Fig. 2C, 2D**). Together, these integrated analyses point towards potent AKT
248 degradation-induced activation of stress MAPK signaling and inflammatory gene signatures.

249

250 **Activation of stress MAPK signaling in response to AKT degradation**

251 To validate the COSMOS predictions, we screened the kinetics of p38 and JNK
252 signaling over a time course in a panel of breast cancer cell lines (**Fig. 4A-C, S6A-C**). Cells
253 exhibited distinct p38 and JNK signaling kinetics and magnitude in response to INY-05-040
254 compared to GDC-0068. Consistently, AKT degradation resulted in more robust induction of
255 p38 α phosphorylation (**Fig. 4A-C, Fig. S6A-C**), supporting the COSMOS-based prediction of
256 differential activity at the level of p38 (also known as MAPK14) when comparing INY-05-040-
257 and GDC0068-specific networks (**Fig. 3B, 3C**).

258 In the screen of BT-474 and T47D breast cancer cells, INY-05-040 induced sustained
259 phosphorylation of the JNK target cJun at Ser⁷³, as well as increased total c-Jun protein levels,
260 which is a marker for JNK activation³⁵ (**Fig. 4A-C**). Particularly at later time points (>96 h), BT-
261 474 cells responded with a near-binary difference in stress MAPK activation in response to AKT
262 degradation compared to catalytic inhibition (**Fig. 4B, 4C**). We therefore tested whether
263 induction of stress MAPK signaling was associated with AKT degrader-induced cytotoxicity. BT-
264 474 and T47D cells were pre-treated with a low-dose (50 nM) of the covalent JNK1/2/3 inhibitor
265 JNK-IN-8 for 24 h, then with either GDC-0068 or INY-05-040 for another 120 h. The two cell
266 lines were chosen for screening as models for a potent (BT-474) versus modest (T47D)
267 cytotoxic response to AKT degradation and a substantially lower magnitude of GDC-0068-
268 induced cell death (fig. S7A). Consistently, the INY-05-040-induced cytotoxic response in T47D
269 cells was neutralized by JNK inhibition (**Fig. 4D, Fig. S7A**). In BT-474 cells, however, combined
270 AKT degradation and JNK inhibition only led to a small, partial rescue of cytotoxicity (**Fig. 4D,**
271 **Fig. S7A**); the increased levels of cleaved PARP, a marker of apoptosis, in BT-474 cells treated
272 with AKT degrader were also not reduced by co-treatment with JNK-IN-8 (**Fig. S7B**). We
273 therefore conclude that although sustained activation of stress MAPK correlates with INY-05-

274 040-induced toxicity, complete ablation of this mechanism is not sufficient to rescue cell viability,
275 suggesting the existence of other contributing factors.

276 **Global cell line screening identifies stress MAPK-associated resistance biomarkers**

277 Given the improved cellular potency of INY-05-040, including robust downstream
278 transcriptional and metabolic changes, we next undertook global cancer cell line profiling to
279 determine whether INY-05-040 causes more potent growth suppression relative to GDC-0068
280 and the first-generation AKT degrader INY-03-041. Across 288 cancer cell lines, spanning a
281 total of 18 different cancer lineages, INY-05-040 exhibited superior growth-inhibitory activity
282 (**Fig. S8A**). This was based on calculation of the drug concentration required to reduce overall
283 growth by 50% (GI50adj, **Fig. 5A**), which includes adjustment for cell number at the start of the
284 assay³⁶. Although GI50adj calculation was possible for all cell lines treated with the second-
285 generation degrader and for 282 cell lines treated with the first-generation degrader, it was not
286 possible for 161 cell lines treated with GDC-0068 due to lack of sufficient growth suppression
287 (**Fig. S8A**). Consequently, the median GI50adj value for GDC-0068 in our screen was higher
288 than 10 μ M, compared to 1.1 μ M for INY-05-040 and 3.1 μ M for INY-03-041.

289 To identify functional biomarkers predictive of sensitivity to INY-05-040 in the 21 breast
290 cancer cell lines profiled, we took advantage of the measured GI50adj values and the
291 corresponding baseline transcriptomic, proteomic and reverse phase protein array (RPPA) data
292 publicly available through the Cancer Dependency Map project (**Fig. 5A**)^{37,38}. We classified
293 breast cancer cells into sensitive, intermediate, and resistant if the measured GI50adj was less
294 than 0.5 μ M, between 0.5 to 1 μ M, and higher than 1 μ M (**Fig. S8B**), respectively. Subsequent
295 unsupervised PCA using either transcriptomic or proteomic datasets revealed a separation of
296 INY-05-040-sensitive from -resistant breast cancer cells, which was not simply driven by ER
297 expression as assessed by PAM50 status (**Fig. 5B**). Except for one mixed-subtype HER2-
298 amplified-luminal breast cancer cell line (DU4475), all examined HER2-amplified and luminal

299 breast cancer cells were sensitive to INY-05-040. This sensitivity was also observed for 4 out of
300 5 breast cancer cells belonging to the basal A subtype. By contrast, only 1 out of 6 basal B
301 breast cancer cell lines were sensitive to INY-05-040, with 4 out of 6 exhibiting overt resistance
302 (**Fig. 5B**).

303 Using the PC1 loadings from the transcriptomic and proteomic data, we then correlated
304 these to the measured GI50adj values. This revealed strong and statistically significant
305 correlations for either comparison, with higher PC1 loadings associated with higher GI50adj
306 values and thus resistance to INY-05-040 (**Fig. 5C, 5D**). To identify the underlying molecular
307 features, we performed GSEA on the two PC1 loadings (transcriptomic and proteomic data).
308 Gene sets that were positively enriched for alongside either PC1 were highly concordant and
309 characterized by strong enrichment for epithelial mesenchymal transition and inflammatory
310 signaling (**Fig. 5E**). Most of these positive enrichments overlapped with those observed upon
311 acute 10-h treatment of T47D breast cancer cells with INY-05-040 (**Fig. 5F**). Based on our
312 mechanistic data on acute JNK activation and sensitivity to INY-05-040, we reasoned that the
313 correlation between inflammatory gene signatures and INY-05-040 resistance in the breast
314 cancer cell panel may reflect an already high baseline JNK activation and thus stress MAPK
315 signaling. Accordingly, we found that both *JNK1* mRNA levels (**Fig. 5G**), JNK1 phosphorylation
316 (Thr^{183/187}) (**Fig. 5H**) and cJun phosphorylation (Ser⁷³) (**Fig. 5I**) exhibited a positive and
317 statistically significant correlation with INY-05-040 GI50adj values.

318 The BT-474 breast cancer cell line, which exhibits a strong cytotoxic response to INY-05-
319 040 (**Fig. 4C, S7A**), had the lowest GI50adj value and the lowest values for markers of baseline
320 JNK1 activation, followed by T47D cells (**Fig. 5H, 5I**). The AKT degrader-induced cell death
321 response in T47D cells was modest compared to that in BT-474 cells and nearly on par with that
322 observed following treatment with GDC-0068 (**Fig. 4C and S7A**). Thus, the relative cytotoxic
323 response to INY-05-040 correlated with the GI50adj-based sensitivity rankings predicted by

324 baseline protein-level measurements of JNK1 activity markers. To test this relationship, we next
325 applied INY-05-040 and GDC-0068 to two distinct breast cancer cell lines, HCC-1395 (TNBC,
326 with loss of *PTEN*) and HCC-1143 (TNBC, with amplification of *AKT1*), that were not part of the
327 initial breast cancer cell line screen. Based on available RPPA data, the two cell lines ranked
328 higher than T47D for baseline JNK1 activation (**Fig. S9A**), and our model would therefore
329 predict a low cytotoxic response to AKT degradation/inhibition, with a lower magnitude relative
330 to T47D cells (**Fig. 4C, S7A**). Consistent with this prediction, both HCC-1395 and HCC-1143
331 exhibited minimal cytotoxicity to either treatment (**Fig. S9B,S9C**), and failed to induce further
332 stress MAPK signaling relative to a higher baseline (**Fig. S9D**). Together, these data
333 demonstrate superior potency of INY-05-040-induced AKT degradation over AKT catalytic
334 inhibition across cancer cell lines, with evidence for a cytotoxic response in the context of low
335 baseline yet potent and sustained induction of stress MAPK signaling in breast cancer cells.

336

337 **Discussion**

338 Targeted protein degradation has emerged as both a therapeutic approach and a
339 powerful experimental tool to evaluate the effects of acute protein depletion on cellular
340 networks. Here we have reported the development of a potent and highly selective second-
341 generation pan-AKT degrader, INY-05-040, which we used as a tool to uncover AKT biology.
342 Using a multiomic approach in breast cancer cell models, we found that AKT degradation led to
343 distinct transcriptomic and metabolomic changes, suppression of downstream AKT signaling,
344 concomitant with activation of stress MAPK signaling. Furthermore, in a set of breast cancer cell
345 lines, low baseline levels of JNK activation were associated with increased sensitivity to AKT
346 degradation.

347 The ongoing search for targeted agents to treat patients with PI3K pathway
348 hyperactivation has focused on the identification of more selective compounds and effective

349 combinations to limit toxicity and improvements in patient selection³⁹. The PI3K α -selective
350 inhibitor alpelisib (PIQRAY®) is approved for the treatment of advanced hormone receptor-
351 positive, HER2-negative breast cancer, in combination with the ER antagonist fulvestrant⁴⁰.
352 Alpelisib (VIJOICE®) is also approved for the treatment of developmental overgrowth disorders
353 collectively known as *PIK3CA*-related overgrowth spectrum (PROS)^{41,42}. Despite this progress,
354 more treatment options are urgently needed for both cancers and diseases of PI3K pathway
355 activation to address issues of resistance and/or poor tolerability. Independent lines of evidence,
356 including the current study, indicate that targeted protein degradation of PI3K pathway
357 components may represent a distinct therapeutic strategy, with the added benefit of sustained
358 inhibition of downstream signaling^{18,43,44}. This property may partly be explained by the inability
359 of various negative feedback mechanisms within the PI3K/AKT pathway to overcome inhibition
360 when a critical downstream transducer is absent. Prolonged cellular stress can also suppress
361 AKT/mTORC1 activity, alongside a more complete shutdown of protein translation, which may
362 contribute to a self-sustained feedforward loop of continued suppression of AKT signaling
363 despite removal of the AKT degrader. This hypothesis is supported by washout screen
364 experiments in which pathway reactivation was not observed or remained low for at least 72 h
365 after degrader removal, in contrast to the corresponding findings with catalytic AKT inhibition
366 with GDC-0068 (**Fig. 1E, Fig. S1G**).

367 Using a network biology framework, COSMOS, we demonstrated how systematic
368 integration of a prior knowledge with context-specific transcriptomic and metabolomic data can
369 be used to identify and subsequently test mechanistic hypotheses on AKT degradation-selective
370 signaling outcomes. This approach identified the stress MAPKs, p38 α (which is encoded by
371 *MAPK14*) and JNK1 (which is encoded by *MAPK8*), as differentially activated in breast cancer
372 cells treated with the AKT degrader INY-05-040. The observed quantitative differences would

373 have been challenging to resolve with conventional approaches, emphasizing the power of
374 computational integration of multiomics data and temporal analyses.

375 The involvement of stress MAPK and inflammatory signaling in the cellular response to
376 AKT degradation was further supported by integration of growth inhibition measurements with
377 publicly available omics data. The observation that the same transcriptional and signaling
378 signatures induced upon degrader treatment of T47D cells were already elevated at baseline in
379 breast cancer cell lines with lower sensitivity to INY-05-040 suggests that low baseline stress
380 MAPK and inflammatory signaling activity may be a prerequisite for potent cell growth
381 suppression following AKT degradation. Our data furthermore suggest that a low baseline yet
382 strong and sustained stress MAPK activation upon AKT degradation predicts cytotoxicity in
383 response to AKT degradation.

384 At present, the precise mechanistic link between AKT degradation and stress MAPK
385 activation remains undescribed. We speculate that ribosomal stress may contribute to the
386 induction of stress MAPKs because AKT and mTORC1 promote ribosome biogenesis through
387 transcriptional and translational mechanisms. Conversely, disruption of any given step in
388 ribosome biogenesis causes ribosomal stress⁴⁵. Accordingly, AKT degradation but not catalytic
389 inhibition leads to a potent and sustained reduction in total ribosomal S6 protein, which would
390 be consistent with the low stability of ribosomal proteins in the absence of functional ribosome
391 formation^{45,46}. Aberrant cholesterol metabolism may also contribute to the cellular stress
392 observed upon AKT degradation. Low cholesterol is linked to increased NF κ B activation and
393 cell death in fibroblasts through a p38 MAPK-dependent mechanism^{47,48}; accordingly, activating
394 transcriptomic signatures for both inflammatory and stress MAPK pathways were strongly
395 enriched for in AKT degrader-treated cells. Additional studies are required to understand this
396 putative crosstalk.

397 Several other AKT degraders have been developed to date, including the VHL-recruiting
398 AZD5363-based AKT degrader MS21¹⁸. Like INY-05-040, MS21 also outperformed its parental
399 AKT kinase inhibitor in cancer cell growth and signaling assays¹⁸. Additional side-by-side
400 comparisons of MS21 and INY-05-040 are needed to determine whether both compounds share
401 similar cellular mechanisms of action downstream of AKT degradation, given the subtle but
402 important differences in their biochemical profiles. The six cell lines identified as more sensitive
403 to AKT degradation with MS21 compared to inhibition with AZD5363 all had lower than average
404 levels of phosphorylated JNK as measured by RPPA¹⁸, consistent with our results. In summary,
405 we demonstrate improved suppression of cancer cell growth with a potent second-generation
406 AKT degrader and illustrate how protein degraders, in combination with integrated systems-level
407 analyses, can be used to uncover new biology of a widely-studied signaling kinase.

408

409

410 **MATERIALS AND METHODS**

411 A complete list of all reagents used in this work is included in the Supplementary Materials
412 (Tables S5-S9).

413 **Biochemical Selectivity Assay**

414 Biochemical selectivity across 468 kinases was measured through the scanMAX kinase
415 assay panel provided through Eurofins Discovery.

416 **Cell Culture**

417 BT-474, T47D, MCF-7, MDA-MB-468, HCC1143, and HCC1395 cells were obtained
418 from ATCC and cultured in RPMI media supplemented with 10% heat inactivated fetal bovine
419 serum without antibiotics at 37 °C in the presence of 5 % CO₂. Cells were maintained in Corning
420 TC-treated 15 cm culture dishes (Corning Cat. # 08-772-24) in 20 mL medium. Medium was
421 replenished every 3 days, until cells reached 70-90% confluence. To passage, cells were
422 washed once with 10 mL PBS and incubated for 5-10 min at 37 °C with 0.25% Trypsin 0.1%
423 EDTA and passaged up to 5 times in the same dish. Cells were maintained in culture for up to
424 one month. Cells were routinely tested for mycoplasma using a Mycoplasma Detection Kit
425 (Lonza Cat. # LT07-218).

426

427 **Cell Death Experiments**

428 T47D and BT-474 cells were plated at 4,000 or 6,000 cells/well in 80 µl RPMI + 10%
429 FBS medium in black-walled clear-bottom 96-well plates (Fisher Cat # 12-566-70). Medium was
430 exchanged the following day with 90 µl medium plus 10 µl of drug containing medium for a 24-h
431 pre-treatment. Two days after plating, medium was exchanged with 80 µl complete medium plus
432 20 µl of drug containing medium. After an additional three days, 100 µl of drug-containing

433 medium was replenished without removing existing medium to prevent nutrient depletion until
434 assay endpoint.

435 HCC1143 and HCC1395 cells were plated at 2,000 or 6,000 cells/well in 80 μ l RPMI +
436 10% FBS medium in black-walled clear-bottom 96-well plates (Fisher Cat # 12-566-70). The
437 following day, medium was exchanged with 90 μ l complete medium plus 10 μ l of drug
438 containing medium. After an additional three days, 100 μ l of drug-containing medium was
439 replenished without removing existing medium, to prevent nutrient depletion until assay
440 endpoint, for a total of 120 hours compound treatment.

441

442 **Cellular Signaling**

443 Depending on the length of the experiment, cells were plated at 150,000-250,000
444 cells/mL (MDA-MB-468), 200,000-300,000 cells/mL (BT-474, T47D) in RPMI medium with 10%
445 serum at 2 mL per well in 6-well treated tissue culture plates (Greiner, Cat. # TCG-657160) and
446 incubated overnight. The next day, medium was exchanged, and cells were treated with the
447 indicated compounds at the appropriate concentration and protein lysates were harvested at the
448 times specified. Time courses were conducted in reverse by drugging cells for the longest time
449 point first, which was followed by drugging cells for the shorter time points such that all samples
450 were collected at the same time. At the time of harvest, cells were washed once with 2 mL of
451 ice-cold PBS and either snap frozen on dry ice and stored at -80 °C or harvested immediately.

452 **RNAseq analysis**

453 Cells were plated at 300,000 cells/mL in RPMI medium with 10% serum at 2 mL per well
454 in 6-well treated tissue culture plates (Greiner, Cat. # TCG-657160) to achieve 75% density the
455 following day and incubated overnight. The following day, media stocks containing indicated
456 compounds were prepared and used to treat all conditions at respective time points, stored at

457 4°C between treatments. After 5 h and 10 h of treatment, wells were washed once with 2 mL ice
458 cold PBS and aspirated completely, snap frozen on dry ice, and stored at -80 °C until all
459 replicates were collected. Three independent biological replicates were plated on sequential
460 days. In parallel, samples were also collected for protein harvest for confirmation of consistent
461 drug effect on cellular signaling.

462 **PRO-seq analysis**

463 T47D cells were seeded at 8×10^6 cells per 15 cm plates (Corning Cat. # 08-772-24) in
464 15 mL medium for PRO-seq samples or at 3×10^6 cells per 10 cm plates (Westnet Cat. #
465 353003) in 8 mL medium for protein samples to achieve 70% confluence. The following day, a
466 stock of drug-containing medium was prepared and used to treat technical triplicates for each
467 condition. Technical triplicate protein replicates treated the same way were collected in parallel.
468 Protein plates were washed once with 8 mL of ice-cold PBS and snap frozen on dry ice, then
469 stored at -80 °C until all replicates were collected.

470 **Metabolomics analysis**

471 Cells were plated at 2×10^6 cells/plate in RPMI medium with 10% in 3 mL per plate in 60
472 mm treated tissue culture plates (Corning, Cat. # 430166) and incubated overnight. The next
473 day, stocks of medium were prepared containing the indicated compounds at the appropriate
474 concentration, and medium was exchanged for drug-containing medium. Three independent
475 biological replicates were performed for metabolomics experiments, each comprising technical
476 triplicates for metabolite plates and technical duplicate of parallel protein samples used to
477 assess suppression of signaling and normalize metabolite levels to total protein content. Due to
478 an apparent loss of potency, the dose of GDC-0068 was increased to 750 nM in Trial 3,
479 compared to 500 nM in Trials 1 and 2, to ensure consistent biochemical signaling suppression
480 across all runs.

481 **Proliferation Assays**

482 T47D, MDA-MB-468, MCF-7 or BT-474 cells were plated in 384 well plates at 250 cells
483 per well. After 24 hours, cells were treated with GDC-0068, AZD5363, MK-2206, ARQ-092, INY-
484 03-041, INY-05-040, INY-05-040-Neg, or VH032 compounds at the indicated concentrations for
485 72 hours. The anti-proliferative effects of these compounds were assessed using the Cell Titer
486 Glo assay kit (Promega Cat. # G7570) following the manufacturer's protocol. EC₅₀ values were
487 determined using GraphPad Prism using nonlinear regression curve fitting.

488 **CellTox Green Cell Death Assay**

489 Cell viability was assayed with a CellTox Green cell death assay. Cells in 96-well plates
490 (ThermoFisher Cat. # 165305) were treated with a 1:1000 dilution (in assay buffer) of CellTox
491 Green dye for 30 min at room temperature, protected from light. Fluorescence intensity,
492 corresponding to binding of CellTox Green dye to double-stranded DNA from dead cells, was
493 measured on a SpectraMax iD3 Microplate Reader (485 nm excitation/520 nm emission) from
494 the bottom, with an integration time of 400 ms and 9 multi-point readings per well. To estimate
495 the total number of cells for subsequent normalization, all wells were subsequently
496 permeabilized with 0.1% Triton X-100 (Fisher Scientific Cat. # BP151-100) and enough CellTox
497 Green reagent to maintain "1X" final concentration. After incubating for 30 min at room
498 temperature protected from light, the final fluorescence intensity was measured as above.
499 Readings from each well were averaged and corrected by subtracting the average background
500 signal from wells with medium and CellTox Green and no cells. The cytotoxicity index was
501 calculated for treatments of interest by dividing background-corrected non-permeabilized
502 readings by the corresponding permeabilized readings to assess the percentage of cell death.
503 Each assay run was quality checked by inclusion of a standard curve of increasing cell number,
504 which was followed by permeabilization and measurement of the CellTox Green signal. All raw

505 data and annotated analysis scripts are available on the associated OSF project website
506 (<https://osf.io/fasqp/>).

507 In parallel, cell health and CellTox Green uptake were also assessed by light
508 microscopy, with image capture on a Keyence BZ-X800 (brightfield and 488 nm) and an ECHO
509 Scope (brightfield only; 10X). These images were used as internal QC and are not incorporated
510 in the final manuscript but have been deposited on the OSF project website
511 (<https://osf.io/fasqp/>) as further supporting evidence.

512 **Immunoblotting**

513 Cells were washed once in 1x PBS then lysed in RIPA buffer (150 mM Tris-HCl, 150 mM
514 NaCl, 0.5% (w/v) sodium deoxycholate, 1% (v/v) NP-40, pH 7.5) containing 0.1% (w/v) sodium
515 dodecyl sulfate, 1 mM sodium pyrophosphate, 20 mM sodium fluoride, 50 nM calyculin, and
516 0.5% (v/v) protease inhibitor cocktail (Sigma-Aldrich Cat. # P8340-5ML) for 15 min. Cell extracts
517 were precleared by centrifugation at 18,800 x g for 10 min at 4 °C. The Bio-Rad DC protein
518 assay was used to assess protein concentration as per the manufacturer's instructions, and
519 sample concentration was normalized using 2x SDS sample buffer. Next, 20 µg of protein
520 lysates and PageRuler Plus (Fisher Cat. # PI26619) prestained protein ladder were resolved on
521 10% acrylamide gels by SDS-polyacrylamide gel electrophoresis and electrophoretically
522 transferred to nitrocellulose membrane (BioRad Cat. # 1620112) at 100 volts for 90 min.
523 Membranes were blocked in 5% (w/v) nonfat dry milk (Fisher Cat# NC9022655/190915ASC) or
524 5% (w/v) bovine serum albumin (Boston Bioproducts Cat. # P-753) in Tris-buffered saline (TBS)
525 for 1 h, then incubated with specific primary antibodies diluted 1:1000 in 5% (w/v) bovine serum
526 albumin in TBS-T (TBS with 0.05% Tween-20) at 4 °C overnight, shaking. The next day,
527 membranes were washed 3 times for 5 min each with TBS-T then incubated for 1 h at room
528 temperature with fluorophore-conjugated secondary antibodies (LI-COR Biosciences) in 5%
529 (w/v) nonfat dry milk, protected from light. The membrane was washed again 3 times for 5 min

530 each with TBS-T, followed by a final 5-min wash in TBS, then imaged with a LI-COR Odyssey
531 CLx Imaging System (LI-COR Biosciences).

532 For blots in Figure S7, medium containing dead or floating cells was collected from each
533 well and centrifuged for 5 min at 300 x rcf. Medium was aspirated, and the pellet lysed in RIPA
534 buffer and combined with protein harvested from corresponding adherent cells as described
535 above.

536 Quantification was performed in ImageStudioLite Software (Licor Biosciences) by
537 drawing rectangles around bands to capture band signal intensities, which were calculated as
538 total pixel intensity minus background pixel intensity. Relative phospho-protein signal was
539 performed for each lane by dividing phospho-protein signal intensity by corresponding total
540 protein signal intensity. Relative AKT signal was calculated by dividing AKT signal intensity by
541 Vinculin signal intensity. Normalization to DMSO samples was performed by dividing relative
542 signal intensity for each condition by the corresponding DMSO signal intensity values. Dotted
543 white lines were used throughout the figures to aid the reader in separating different treatments
544 and not as an indicator of lane splicing, unless indicated in the figure legend.

545 **MOLT4 Cell Culture and Sample Preparation for Proteomics Analysis**

546 MOLT4 cells (T lymphoblast cell line established from a 19-year-old male patient with
547 acute lymphoblastic leukemia in relapse) were grown in RPMI-1640 media including 2mM L-
548 glutamine (Gibco) and supplemented with 10% fetal bovine serum (Gibco) in a 37°C incubator
549 with 5% CO₂. MOLT4 cells were treated with DMSO or 250 nM INY-05-040 for 4 h. Cells were
550 harvested by centrifugation and lysis buffer (8 M urea, 50 mM NaCl, 50 mM 4-(2hydroxyethyl)-1-
551 piperazineethanesulfonic acid (EPPS) pH 8.5) with 1x cOmplete protease inhibitor (Roche) and
552 1x PhosphoStop (Roche) was added. Cells were subsequently homogenized by 20 passes
553 through a 21-gauge (1.25 inch long) needle to achieve a cell lysate with a protein concentration
554 between 0.5-4 mg/mL. The homogenized sample was clarified by centrifugation at 20,000 x g

555 for 10 min at 4°C. A Bradford assay was used to determine the final protein concentration in the
556 cell lysate. 200 µg protein for each sample were reduced, alkylated precipitated using
557 methanol/chloroform and dried as previously described⁴⁹. Precipitated protein was resuspended
558 in 4 M urea, 50 mM HEPES pH 7.4 then diluted to 1 M urea with the addition of 200 mM EPPS
559 pH 8 for digestion with LysC (1:50; enzyme:protein) for 12 h at room temperature. The LysC
560 digestion was diluted to 0.5 M urea, 200 mM EPPS pH 8 and digested with trypsin (1:50;
561 enzyme:protein) for 6 h at 37°C. Tandem mass tag (TMT) reagents (Thermo Fisher Scientific)
562 were dissolved in anhydrous acetonitrile (ACN) according to the manufacturer's instructions.
563 Anhydrous ACN was added to each peptide sample to a final concentration of 30% v/v, and
564 labeling was induced with the addition of TMT reagent to each sample at a ratio of 1:4
565 peptide:TMT label. The 11-plex labeling reactions were performed for 1.5 h at room temperature
566 and the reaction quenched by the addition of 0.3% hydroxylamine for 15 minutes at room
567 temperature. The sample channels were combined at a 1:1 ratio, desalted using C18 solid
568 phase extraction cartridges (Waters) and analyzed by LC-MS for channel ratio comparison.
569 Samples were combined using the adjusted volumes determined in the channel ratio analysis
570 and dried down in a speed vacuum. The combined sample was resuspended in 1% formic acid
571 and acidified to pH 2-3 before being subjected to desalting with C18 SPE (Sep-Pak, Waters).
572 Samples were offline fractionated into 96 fractions by high pH reverse-phase HPLC (Agilent
573 LC1260) through an Aeris peptide XB-C18 column (phenomenex) with mobile phase A
574 containing 5% acetonitrile and 10 mM NH₄HCO₃ in LC-MS grade H₂O, and mobile phase B
575 containing 90% acetonitrile and 10 mM NH₄HCO₃ in LC-MS grade H₂O (both pH 8.0). The 96
576 resulting fractions were pooled in a non-contiguous manner into 24 fractions, desalted using
577 solid phase extraction plates (SOLA, Thermo Fisher Scientific), and subjected to mass
578 spectrometry analysis.

579 Data were collected using an Orbitrap Fusion Lumos mass spectrometer (Thermo Fisher
580 Scientific, San Jose, CA, USA) coupled with a Proxeon EASY-nLC 1200 LC pump (Thermo
581 Fisher Scientific). Peptides were separated on a 50 cm and 75 μm inner diameter Easyspray
582 column (ES803a, Thermo Fisher Scientific). Peptides were separated using a 190 min gradient
583 of 6 – 27% acetonitrile in 1.0% formic acid with a flow rate of 300 nL/min. Each analysis used an
584 MS3-based TMT method as described previously⁵⁰. The data were acquired using a mass range
585 of m/z 340 – 1350, resolution 120,000, AGC target 5×10^5 , maximum injection time 100 ms,
586 dynamic exclusion of 120 seconds for the peptide measurements in the Orbitrap. Data
587 dependent MS2 spectra were acquired in the ion trap with a normalized collision energy (NCE)
588 set at 35%, AGC target set to 1.8×10^4 and a maximum injection time of 120 ms. MS3 scans
589 were acquired in the Orbitrap with a HCD collision energy set to 55%, AGC target set to 2×10^5 ,
590 maximum injection time of 150 ms, resolution at 50,000 and with a maximum synchronous
591 precursor selection (SPS) precursors set to 10.

592 Proteome Discoverer 2.4 (Thermo Fisher) was used for .RAW file processing and
593 controlling peptide and protein level false discovery rates, assembling proteins from peptides,
594 and protein quantification from peptides. MS/MS spectra were searched against a Swissprot
595 human database (February 2020) with both the forward and reverse sequences. Database
596 search criteria are as follows: tryptic with two missed cleavages, a precursor mass tolerance of
597 10 ppm, fragment ion mass tolerance of 0.6 Da, static alkylation of cysteine (57.02146 Da),
598 static TMT labeling of lysine residues and N-termini of peptides (229.16293 Da), variable
599 phosphorylation of serine, threonine and tyrosine (79.966 Da), and variable oxidation of
600 methionine (15.99491 Da). TMT reporter ion intensities were measured using a 0.003 Da
601 window around the theoretical m/z for each reporter ion in the MS3 scan. Peptide spectral
602 matches with poor quality MS3 spectra were excluded from quantitation (summed signal-to-
603 noise across 11 channels < 100 and precursor isolation specificity < 0.5). Only proteins

604 containing at least two unique peptides identified in the experiment were included in the final
605 quantitation. Reporter ion intensities were normalized and scaled using in-house scripts in the R
606 framework⁵¹.

607 The proteomics experiment was part of a standard screening workflow for new degrader
608 molecules and therefore only has triplicate measurements for the control-treated samples and a
609 single measurement for the degrader molecule. This precludes formal statistical analyses of
610 fold-changes beyond confirming that the expected target molecules (AKT1, AKT2, AKT3 in this
611 case) have been depleted.

612 **RNA sequencing analysis**

613 Snap-frozen cells were thawed on ice and RNA extracted with Takara's Nucleospin RNA
614 Plus kit (Takara Cat. # 740984.50) according to the manufacturer's instructions. RNA integrity
615 was assessed for quantity and purity by Nanodrop 1000. Samples were submitted to Novogene
616 for integrity assessment (Agilent 2100 analysis), mRNA library preparation (unstranded), and
617 paired-end (150 bp) sequencing on a NovaSeq S4 flow cell.

618 Raw read processing was performed with the Nextflow (version 20.07.1) nf-core RNAseq
619 pipeline (version 1.4.2)⁵², with Spliced Transcripts Alignment to a Reference (STAR)⁵³ for read
620 alignment to the human genome (Homo_sapiens.GRCh38.96.gtf) and featureCounts⁵⁴ for
621 counting of mapped reads (multimapped reads were discarded). All subsequent data processing
622 was performed in R, with differential gene expression analysis following the limma-voom
623 method⁵⁵. Filtering of low gene expression counts was performed with the *TCGAbiolinks*
624 package with quantile value 0.75 (chosen empirically based on the observed count distribution).
625 Next, read count normalization was performed with the trimmed mean of M (TMM) method⁵⁶.
626 PCA was done using the *PCAtools* package. The mean-variance relationship was modelled with
627 voom(), which was followed by linear modelling and computation of moderated t-statistics using

628 the `lmFit()` and `eBayes()` functions in the *limma* package⁵⁵. Experimental replicate was included
629 as a batch effect term in the model. The associated p-values for assessment of differential gene
630 expression were adjusted for multiple comparisons with the Benjamini-Hochberg method at a
631 false-discovery rate (FDR) = 0.05⁵⁷. Adjustments were performed separately for each contrast of
632 interest. Subsequent gene annotations were performed with *BioMart* within R⁵⁸, using the
633 associated ENSEMBL Gene IDs as key values. Intersection plots and heatmaps were
634 generated using the *ComplexHeatmap* package⁵⁹. Clustering was performed using the `Ward.D2`
635 method. Columns were clustered according to Euclidean distance, and rows (genes) were
636 clustered according to Spearman's correlation (meaning patterns of change as opposed to
637 maximum values).

638 The *msigdb* package was used to retrieve the indicated gene signatures. GSEA was
639 performed with the *fgsea* package⁶⁰, using the list of all genes ranked according to their *t*
640 statistic for a comparison of interest. The choice to use *the t* statistic ensures that the gene
641 ranking considers signal magnitude (fold-change) as well as uncertainty of estimation.
642 Normalized enrichment values and associated p-values were calculated with the
643 `fgseaMultilevel()` function, using default settings. The normalized enrichment score computed by
644 the algorithm corresponds to the enrichment score normalized to mean enrichment of random
645 samples, using the same gene set size.

646 The voom-normalized counts were used to predict transcription factor activities with
647 DoRothEA²⁴, choosing regulons within confidence groups "A", "B" and "C" (low-confidence
648 regulons in groups "D" and "E" were therefore not considered). As per the developer's
649 recommendations, the "minsize" argument in the options was set to "5", and "eset.filter" was set
650 to "FALSE". Exact details can be retrieved from the deposited code. Annotated scripts for all
651 analysis steps post-read processing are provided on the OSF project webpage
652 (<https://osf.io/3f2m5/>).

653 Precision nuclear run-on sequencing (PRO-seq) analysis

654 To harvest cell pellets for PRO-seq analysis, cells were washed once with 8 mL room
655 temperature 1X PBS and trypsinized for 5 min. Trypsin was quenched with ice cold DMEM +
656 10% FBS and cells were collected in a 50 mL conical tube and placed onto ice immediately.
657 Cells were spun at 300 x g for 4 min at 4°C, supernatant was removed, and cells were
658 resuspended in 250 μ L Buffer W (10 mM Tris-Cl, pH 8.0; 10 mM KCl; 250 mM Sucrose; 5 mM
659 MgCl₂; 1 mM EGTA; 0.5 mM DTT; 10 % (v/v) Glycerol; Protease inhibitor tablet (EDTA-free),
660 0.02% SUPERase-IN RNase inhibitor) to obtain a single-cell suspension by pipetting. 10 mL of
661 Buffer P (10 mM Tris-Cl, pH 8.0; 10 mM KCl; 250 mM Sucrose; 5 mM MgCl₂; 1 mM EGTA; 0.1
662 % (v/v) Igepal CA-630; 0.5 mM DTT; 0.05 % (v/v) Tween-20; 10 % (v/v) Glycerol; Protease
663 inhibitor tablet (EDTA-free), 0.02% SUPERase-IN RNase inhibitor) was added and cells were
664 incubated on ice for 5 min and spun at 400 x g for 4 min at 4 °C. Supernatant was removed and
665 Buffer W was added and pipetted gently 2-3 times to resuspend cells. An additional 9 mL of
666 Buffer W was added to each tube, and cells were spun at 400 x g for 4 min at 4 °C. An
667 additional wash with Buffer W was completed as above and supernatant was decanted so cell
668 pellets were not disturbed. Pellets were resuspended in Buffer F (50 mM Tris-Cl, pH 8.0; 40 %
669 (v/v) glycerol; 5 mM MgCl₂; 1.1 mM EDTA; 0.5 mM DTT, and SUPERase-IN RNase inhibitor)
670 and transferred to a 1.5 mL tube. The 50 mL tube was rinsed again with 250 μ l of Buffer F and
671 added to the corresponding 1.5 mL tube for a final volume of 500 μ l per sample. 10 μ l was
672 reserved for counting after dilution 1:10 and 1:20 in PBS, both with and without trypan blue to
673 calculate the fraction of permeabilized cells. Cells were diluted to 1 x 10⁶ permeabilized cells per
674 100 μ l and a total of 5 x 10⁶ cells were aliquoted in 500 μ l of Buffer F and snap frozen in liquid
675 nitrogen and stored at -80°C until further processing. RNase-free water was used to make all
676 reagents and solutions, and solutions were filter sterilized with 0.2 μ M filters into RNase-free

677 plastic bottles. Two independent biological replicates were collected, alongside the
678 corresponding protein samples to confirm drug action at the signaling level.

679 Aliquots of frozen (-80 °C) permeabilized cells were thawed on ice and pipetted gently to
680 fully resuspend. Aliquots were removed and permeabilized cells were counted using a Logos
681 Biosystems Luna II instrument. For each sample, 1 million permeabilized cells were used for
682 nuclear run-on, with 50,000 permeabilized *Drosophila* S2 cells added to each sample for
683 normalization. Nuclear run-on assays and library preparation were performed essentially as
684 previously described⁶¹ with the following modifications: 2X nuclear run-on buffer consisted of
685 (10 mM Tris (pH 8), 10 mM MgCl₂, 1 mM DTT, 300 mM KCl, 40uM/ea biotin-11-NTPs (Perkin
686 Elmer), 0.8 U/μL SuperaseIN (Thermo), 1% sarkosyl). Run-on reactions were performed at 37
687 °C. Adenylated 3' adapter was prepared using the 5' DNA adenylation kit (NEB) and ligated
688 using T4 RNA ligase 2, truncated KQ (NEB, per manufacturer's instructions with 15% PEG-
689 8000 final) and incubated at 16 °C overnight. 180 μL of betaine blocking buffer (1.42 g of
690 betaine brought to 10 mL with binding buffer supplemented with 0.6 μM blocking oligo
691 (TCCGACGATCCCACGTTCCCGTGG/3InvdT/)) was mixed with the ligation reactions and
692 incubated 5 min at 65°C and 2 min on ice prior to addition of streptavidin beads. After T4
693 polynucleotide kinase (NEB) treatment, beads were washed once each with high salt, low salt,
694 and blocking oligo wash (0.25X T4 RNA ligase buffer (NEB), 0.3 μM blocking oligo) solutions
695 and resuspended in 5' adapter mix (10 pmol 5' adapter, 30 pmol blocking oligo, water). The 5'
696 adapter ligation was as previously described⁶¹ but contained 15% PEG-8000. Eluted cDNA was
697 amplified for 5 cycles (NEBNext Ultra II Q5 master mix (NEB) with Illumina TruSeq PCR primers
698 RP-1 and RPI-X) following the manufacturer's suggested cycling protocol for library
699 construction. The product (preCR) was serially diluted and used for test amplification to
700 determine the optimal PCR conditions for the final libraries. The pooled libraries were paired-
701 end sequenced using the Illumina NovaSeq platform.

702 All custom scripts described herein are available on the AdelmanLab Github
703 (https://github.com/AdelmanLab/NIH_scripts). Using a custom script (trim_and_filter_PE.pl),
704 FASTQ read pairs were trimmed to 41bp per mate, and read pairs with a minimum average
705 base quality score of 20 retained. Read pairs were further trimmed using cutadapt 1.14 to
706 remove adapter sequences and low-quality 3' bases (--match-read-wildcards -m 20 -q 10). R1
707 reads, corresponding to RNA 3' ends, were then aligned to the spiked in *Drosophila* genome
708 index (dm3) using Bowtie 1.2.2 (-v 2 -p 6 --best --un), with those reads not mapping to the spike
709 genome serving as input to the primary genome alignment step (using Bowtie 1.2.2 options -v 2
710 --best). Reads mapping to the hg38 reference genome were then sorted with samtools 1.3.1 (-n)
711 and subsequently converted to bedGraph format using a custom script (bowtie2stdBedGraph.pl)
712 that counts each read once at the exact 3' end of the nascent RNA. Because R1 in PRO-seq
713 reveals the position of the RNA 3' end, the "+" and "-" strands were swapped to generate
714 bedGraphs representing 3' end positions at single nucleotide resolution.

715 Annotated transcription start sites were obtained from human (GRCh38.99) GTFs from
716 Ensembl. After removing transcripts with {immunoglobulin, Mt_tRNA, Mt_rRNA} biotypes, PRO-
717 seq signal in each sample was calculated in the window from the annotated TSS to +150 nt
718 downstream, using a custom script (make_heatmap.pl). Given good agreement between
719 replicates and similar return of spike-in reads, bedGraphs were merged within conditions and
720 depth-normalized to generate bigwig files binned at 10 bp.

721 The corresponding paired-end RNA-seq reads were mapped to the hg38 reference
722 genome with HISAT2 v2.2.1 (--known-splicesite-infile). To select gene-level features for
723 differential expression analysis and for pairing with PRO-seq data, we assigned a single,
724 dominant TSS and transcription end site (TES) to each active gene. This was accomplished
725 using a custom script, get_gene_annotations.sh (available at
726 <https://github.com/AdelmanLab/GeneAnnotationScripts>), which uses RNAseq read abundance
727 and PRO-seq R2 reads (RNA 5' ends) to identify dominant TSSs, and RNAseq profiles to define

728 most commonly used TESSs. RNAseq and PRO-seq data from all conditions were used for this
729 analysis, to capture gene activity in these samples. Reads were summed within the TSS to TES
730 window for each active gene using the `make_heatmap` script
731 (https://github.com/AdelmanLab/NIH_scripts), which counts each read once at the exact 3' end
732 location of the nascent RNA.

733 All subsequent processing of the PRO-seq count data were as described above for the
734 RNAseq count data. Filtering of low counts was performed with the *TCGAbiolinks* package with
735 quantile value 0.1.

736 **Metabolomics analysis**

737 For metabolite extraction, media was aspirated and cells were washed once with ice-
738 cold PBS on wet ice. Ice-cold 80% (v/v) mass spectrometry-grade methanol was added, the
739 plate was transferred to dry ice and scraped, and the resulting solution was collected. Protein
740 samples were collected in duplicate for normalization to protein content and signaling validation
741 as described above. Insoluble material was pelleted by centrifugation at 20,000 x g for 5 min,
742 and the resulting supernatant was evaporated under nitrogen gas. Samples were resuspended
743 in 20 mL HPLC-grade water for LC/MS analysis.

744 For polar metabolite profiling, 5 μ L from each sample were injected and analyzed using
745 a 5500 QTRAP hybrid triple quadrupole mass spectrometer (AB/SCIEX) coupled to a
746 Prominence UFLC HPLC system (Shimadzu) with HILIC chromatography (Waters Amide
747 XBridge), by selected reaction monitoring (SRM) with polarity switching. A total of 295
748 endogenous water-soluble metabolites were targeted for steady-state analyses. Electrospray
749 source voltage was +4950 V in positive ion mode and -4500 V in negative ion mode. The dwell
750 time was 3 ms per SRM transition 32. Peak areas from the total ion current for each metabolite
751 were integrated using MultiQuant v2.1.1 software (AB/SCIEX).

752 Prior to differential abundance analysis, the raw metabolomics data were preprocessed
753 as follows. Untrusted metabolites were removed from the datasets, including SBP, shikimate,
754 shikimate-3-phosphate, spermidine, spermine, succinyl-CoA-methylmalonyl-CoA-nega,
755 trehalose-6-phosphate, trehalose-sucrose, malonyl-CoA-nega, N-acetyl spermidine, N-acetyl
756 spermine, acetylputrescine, NAD+_nega, NADH-nega, NADP+_nega, NADPH-nega, O8P-O1P,
757 OBP, propionyl-CoA-neg, putrescine, acetoacetyl-CoA_neg, acetyl-CoA_neg, cellobiose,
758 coenzyme A_neg, glutathione, glutathione disulfide-posi. Next, metabolites with low peak
759 intensities (<10,000) across at least 50% of the samples were removed. Finally, all metabolites
760 with 0 intensity in more than 3 samples were also removed, and any metabolites with 0 intensity
761 in < 3 samples were removed in the final differential abundance analysis steps.

762 Metabolomics data normalized to matched protein samples from three independent
763 experiments, each including three separate cell cultures per treatment, were combined into one
764 dataset. Metabolites with missing (“NA”) or negative values in at least one trial were removed,
765 resulting in 169 metabolites included in the final analyses. These were processed for differential
766 abundance testing using the limma-voom method, with quantile normalization due to significant
767 heteroscedascity. Subsequent linear modelling and computation of moderated *t*-statistics was
768 performed with *lmFit()* and *eBayes()* as for the RNAseq data, including experimental replicate as
769 blocking factor due to a noticeable batch effect. Heatmap generation and clustering of
770 differentially abundant metabolites was performed as described for the RNAseq data.

771 **Causal Oriented Search of Multi-Omic Space (COSMOS)**

772 The RNAseq input data for COSMOS consisted of transcription factor *t* values from
773 DoRothEA and the *limma-voom*-based *t* statistic for all genes, irrespective of significance, for a
774 given contrast of interest (GDC-0068 compared to DMSO; INY-05-040 compared to DMSO).
775 The latter served as additional constraints on the solver. Metabolite data for COSMOS
776 consisted of the *limma-voom*-based *t* statistic for metabolites with unadjusted p-value ≤ 0.05 ,

777 resulting in 58 metabolites for GDC-0068 and 77 metabolites for INY-05-040. The decision to
778 use unadjusted p-values for filtering was made a priori due to well-known high correlation
779 across groups of metabolites, thus making the resulting corrections for multiple comparisons
780 overly restrictive. Metabolite names had to be mapped to their corresponding PubChem ID,
781 which was facilitated by the R packages *KEGGREST* and *webchem*⁶².

782 Exact code for generation of both RNAseq and metabolite values in the correct format
783 for COSMOS, as well as extensive details on all required installations and subsequent code for
784 running COSMOS on a high-performance computer cluster, are provided on the accompanying
785 OSF project page (<https://osf.io/tdvur/>). Briefly, the algorithm relies on CARNIVAL's Integer
786 Linear Programming (ILP) optimization, which was rerun multiple times for each dataset to
787 determine the most consistent network predictions. Settings for each run, including the resulting
788 network gap values, are provided in an accompanying table on the OSF project page.
789 Differences included explicit indication of AKT1/2 inhibition (AKT3 was not expressed in T47D
790 cells) as well as shuffling of individual *t* values for the background transcriptome, thus artificially
791 forcing the solver to initiate the optimization from different starting points.

792 A “forward” optimization run to connect deregulated transcription factors (“signaling”
793 input) as starting points to metabolites was performed first, followed by a “backward”
794 optimization run connecting metabolites to signaling components. These optimization runs were
795 used as the basis for the actual forward and final runs defining the output of the algorithm. Time
796 limits for solving were set empirically, ensuring that the gap values of the resulting networks
797 were $\leq 5\%$ (indicative of a good fit). This was achieved for all runs except for one backward run
798 (gap = 9.68%) using GDC-0068 input data. For each network run, we have provided the
799 COSMOS script and its output as separate text files, including all run-specific settings and final
800 gap values (<https://osf.io/tdvur/>).

801 Subsequent network analysis and visualization was performed in R, using the rCy3⁶³
802 package to interface with Cytoscape⁶⁴. For the final visualization, a filter was applied such that
803 text was only displayed for nodes with betweenness values of ≥ 0.05 , the size of the text is
804 indicative of the degree, and the color of the node indicative of its COSMOS-derived activation
805 value. Betweenness is a measure of the number of shortest paths going through a node, or how
806 much a node acts as point of connection or information transmission³¹.

807 **Cancer Cell Line Growth Inhibition Screen**

808 The high throughput cell line screen was outsourced to Horizon by Astra Zeneca. A
809 detailed description of the protocol, alongside cell-line specific culture conditions and GI50 curve
810 fits, are included on the OSF project webpage (<https://osf.io/us45v/>). Briefly, the 288 cell lines
811 were thawed and expanded until they reached their expected doubling times, at which point the
812 screening was begun. Cells were seeded in 25 μ L of growth media in black 384-well tissue
813 culture and equilibrated at 37°C and 5% CO₂ for 24 h before treatment. At the time of treatment,
814 a set of assay plates were collected for initial (V₀) measurements of ATP (used as proxy for
815 viability) using the luminescence-based CellTiter Glo 2.0 (Promega) assay and an Envision
816 plate reader (Perkin Elmer). Compounds were transferred to the remaining treatment plates
817 using an Echo acoustic liquid handling system; 25 nL of each compound was added at the
818 appropriate concentration for all dose points. Plates were incubated with compound for 6 days,
819 and ATP was measured with CellTiter Glo. Data points were collected through automated
820 processes, subjected to quality control, and analyzed with Horizon’s proprietary software.

821 Horizon utilizes Growth Inhibition (GI) as a measure of cell growth. The GI percentages
822 are calculated by applying the following test and equation:

$$823 \quad \textit{If } T < V_0 : 100 * (1 - (T - V_0) / V_0)$$

$$824 \quad \textit{If } T \geq V_0 : 100 * (1 - (T - V_0) / (V - V_0))$$

825 where T is the signal measure for a test drug, V is the untreated/vehicle-treated control
826 measure, and V_0 is the untreated/vehicle control measure at time zero (see above). This
827 formula is derived from the growth inhibition calculation used in the National Cancer Institute's
828 NCI-60 high throughput screen.

829 Publicly available transcriptomic, proteomic and RPPA data and the relevant metadata
830 for breast cancer cells of interest were retrieved from DepMap using the *depmap* R package
831 (doi: 10.18129/B9.bioc.depmap), with access to the following data versions: 21Q1 for metadata
832 and transcriptomic data; 20Q2 for proteomic data; 19Q3 for RPPA. PCA, GSEA, hierarchical
833 clustering and heatmap generation as part of subsequent integration with experimental GI50adj
834 data were performed as described for RNA sequencing analysis. RNAseq data were obtained
835 as transcripts per million (TPM) and were subjected to quantile-based filtering (quantile
836 threshold = 0.25) using the *TCGAbiolinks* package⁶⁵ to remove genes with low expression. We
837 used non-parametric Spearman's correlation to measure the strength of association between
838 variables of interest. GI50adj values were log-transformed (base10) for visualization. For RPPA
839 data, all antibodies labeled with "Caution" were excluded from analysis and the remaining
840 antibody measurements were converted to z-scores prior to visualization.

841 **Pharmacokinetic and Pharmacodynamic Analyses in BT474C Xenografts**

842 Plasma concentrations of GDC-0068, INY-05-040, and INY-03-041 were evaluated over
843 a period of 24 hours. Blood samples were drawn 0.5, 2, 6, 12, and 24 hours following a single
844 dose of GDC-0068 at 12.5 mg/kg, INY-05-040 25 mg/kg, or INY-03-041 25 mg/kg. BT474C
845 pharmacodynamic animal studies were conducted according to AstraZeneca's Global Bioethics
846 Policy in accordance with the PREPARE and ARRIVE guidelines. Female nude mice were
847 surgically implanted with a 0.36 mg/60d 17 β -estradiol pellet (Innovative Research of America)
848 into the left subcutaneous flank. The following day, BT474C cells were implanted at 5 x 10⁶ cells
849 per mouse (suspended in 50% DMEM:50% Matrigel) into the right subcutaneous flank. Mouse

850 weights were monitored twice weekly up until dosing, after which mouse weights were
851 monitored daily. Tumors were measured twice weekly by caliper, with tumor volumes calculated
852 using the formula:

853

854
$$\text{Volume} = (\pi \times \text{Maximum measure (Length or Width)} \times \text{Minimum measure (Length or Width)} \times$$

855
$$\text{Minimum measure (Length or Width)}) / 6000$$

856 The experiments were performed on adult mice weighing more than 18 g at time of first
857 procedure. Mice were randomized by tumor volume into either control or treatment groups when
858 average tumor volume reached 0.5 cm³. Tumor volumes were excluded if outside of the desired
859 range (range used was 0.191-0.851 cm³ with an average of 0.354 cm³).

860 GDC-00068 was dosed perorally twice a day for 4 days at 12.5 mg/kg (5 mL/kg)(0.5%
861 HPMC, 0.1% Tween 80). INY-05-040 and INY-03-041 were dosed for 4 days as a once daily
862 intraperitoneal injection at 25mg/kg (5mL/kg) (10% DMSO/20% Captisol, pH 5.0 with gluconic
863 acid). On the final day of dosing, 4 h after dosing AM dose, mice were humanely killed, and
864 tumor tissue was collected and immediately snap frozen in liquid nitrogen before storage at -
865 80°C.

866 Protein was extracted from snap-frozen tumor fragments by adding 900 µL of extraction
867 buffer (20 mM Tris at pH7.5, 137 mM NaCl, 10% Glycerol, 50 mM NaF, 1 mM Na₃VO₄, 1%
868 SDS, 1% NP40 substitute) with complete protease inhibitor cocktail (Roche Cat. #11836145001;
869 1 tablet per 50 mL). Samples were homogenized twice for 30 seconds at 6.5m/s in a fast-prep
870 machine with an incubation at 4°C for 5 min between runs. Lysates were sonicated in a chilled
871 Diagenode Bioruptor for two cycles (setting: HIGH) of 30 s ON/30s OFF. Lysates were cleared
872 twice by centrifugation and protein concentrations were estimated with the Pierce BCA Protein
873 Assay Kit (Thermo Fisher Scientific Cat. # 23227). Approximately 40 µg of protein was run on a
874 NuPAGE 4–12% Bis-Tris gel (Thermo Fisher Scientific) using standard methods. Following
875 protein separation, proteins were transferred onto nitrocellulose membranes using dry transfer

876 with iBlot2 (Thermo Fisher Scientific #IB21001). Primary antibodies were diluted in Tris-buffered
877 saline (TBS)/0.05% Tween (TBS/T) supplemented with 5% Marvel and incubated overnight at 4
878 °C. The membranes were washed three times for 15 min each in 20 mL of TBS/T. A secondary
879 horseradish peroxidase (HRP)-linked antibody was diluted 1:2000 in TBS/T supplemented with
880 5 % Marvel and incubated for 1 h at room temperature. The membranes were washed three
881 times for 15 min each in 20 mL of TBS/T, and signals were detected using chemiluminescent
882 SuperSignal West Dura Extended Duration Substrate (Thermo Fisher Scientific).

883 **Statistics and Reproducibility**

884 Based on the Statistical Health Check and Principles of Good Statistical Practice,
885 Cohen's D was used to estimate the required number of animals for *in vivo* experiments, taking
886 into account the variability of the assay and the expected effect size. In this case, n of 6 mice
887 was determined as the appropriate sample size for the endpoint.

888 Sample size for other experiments was not pre-determined. Statistical analyses on
889 multidimensional datasets are detailed in the relevant sections. To avoid the pitfalls of
890 dichotomous significance testing on conventional, low-throughput biological datasets, we used
891 estimation statistics (Data Analysis using Bootstrap-Coupled ESTimation)⁶⁶ for data in Figure 4
892 and Figure S9. The default settings were used (5000 resamples, BCa bootstrap)⁶⁶. A key
893 advantage of this approach is the ability to focus on effect sizes and relative confidence
894 intervals derived from bootstrapping; however, we note that the small sample size of the typical
895 cell biological experiment is a general limitation also when it comes to reliable bootstrapping.
896 Nevertheless, the observation of similar trends across independent experiments (for example,
897 compare Figure S7A to Figure 4) gives us confidence in our conclusions.

898 The exact number of technical and biological replicates are specified in the relevant
899 figure legends. We use biological replicates to refer to independent experimental repeats or
900 tumor samples from different mice. Technical replicates refer to individual samples exposed to

901 the same treatment within the same experimental replicate. The biological responses deduced
902 from the Western blots shown in Figures 1 and 4 were reproduced across independent
903 biological contexts (Figures S1 and S6, respectively); for all other Western blots performed in
904 T47D cells only, all independent experimental replicates are included in the Supplementary
905 Materials as indicated. Raw Western blot images are available on the OSF project webpage:
906 <https://osf.io/maq7k/>.

907

908 Supplementary Materials

909 Materials and Methods

910 Figs. S1-S9

911 Tables S1-S9

912 **References and Notes**

913

- 914 1. Manning, *et al.* AKT/PKB Signaling: Navigating the Network. *Cell* **169**, 381–405 (2017).
- 915 2. Sanchez-Vega, *et al.* Oncogenic Signaling Pathways in The Cancer Genome Atlas. *Cell*
916 **173**, 321-337.e10 (2018).
- 917 3. Castel, *et al.* *The present and future of PI3K inhibitors for cancer therapy. Nature Cancer*
918 vol. 2 587–597 (2021).
- 919 4. Turner, *et al.* Genomically amplified Akt3 activates DNA repair pathway and promotes
920 glioma progression. *Proc. Natl. Acad. Sci.* **112**, 3421–3426 (2015).
- 921 5. Davies, *et al.* A novel AKT3 mutation in melanoma tumours and cell lines. *Br. J. Cancer*
922 **99**, 1265–1268 (2008).
- 923 6. Hyman, *et al.* AKT inhibition in solid tumors with AKT1 mutations. *J. Clin. Oncol.* **35**,
924 2251–2259 (2017).
- 925 7. Nitulescu, *et al.* Akt inhibitors in cancer treatment: The long journey from drug discovery
926 to clinical use (Review). *Int. J. Oncol.* **48**, 869–885 (2016).
- 927 8. Uhlenbrock, *et al.* Structural and chemical insights into the covalent-allosteric inhibition of
928 the protein kinase Akt †. (2019) doi:10.1039/c8sc05212c.
- 929 9. Oliveira, *et al.* FAIRLANE, a double-blind placebo-controlled randomized phase II trial of
930 neoadjuvant ipatasertib plus paclitaxel for early triple-negative breast cancer. *Ann. Oncol.*
931 **30**, 1289–1297 (2019).
- 932 10. Turner, *et al.* BEECH: a dose-finding run-in followed by a randomised phase II study
933 assessing the efficacy of AKT inhibitor capivasertib (AZD5363) combined with paclitaxel
934 in patients with estrogen receptor-positive advanced or metastatic breast cancer, and in a
935 PIK3CA . *Ann. Oncol. Off. J. Eur. Soc. Med. Oncol.* **30**, 774–780 (2019).
- 936 11. Huck, *et al.* *Recent progress towards clinically relevant ATP-competitive Akt inhibitors.*

- 937 *Bioorganic and Medicinal Chemistry Letters* vol. 27 2838–2848 (2017).
- 938 12. Martorana, *et al.* *AKT Inhibitors: New Weapons in the Fight Against Breast Cancer?*
939 *Frontiers in Pharmacology* vol. 12 546 (2021).
- 940 13. Nalawansha, *et al.* PROTACs: An Emerging Therapeutic Modality in Precision Medicine.
941 *Cell Chem. Biol.* **27**, 998–1014 (2020).
- 942 14. Burslem, *et al.* Proteolysis-Targeting Chimeras as Therapeutics and Tools for Biological
943 Discovery. *Cell* **181**, 102–114 (2020).
- 944 15. Konstantinidou, *et al.* PROTACs– a game-changing technology. *Expert Opin. Drug*
945 *Discov.* **14**, 1–14 (2019).
- 946 16. Cromm, *et al.* Targeted Protein Degradation: from Chemical Biology to Drug Discovery.
947 *Cell Chem. Biol.* **24**, 1181–1190 (2017).
- 948 17. Huang, *et al.* A Chemoproteomic Approach to Query the Degradable Kinome Using a
949 Multi-kinase Degradation. *Cell Chem. Biol.* **25**, 88-99.e6 (2018).
- 950 18. Xu, *et al.* AKT degradation selectively inhibits the growth of PI3K/PTEN pathway mutant
951 cancers with wild-type KRAS and BRAF by destabilizing Aurora kinase B. *Cancer Discov.*
952 *candisc.0815.2020* (2021) doi:10.1158/2159-8290.cd-20-0815.
- 953 19. Yu, *et al.* Design, Synthesis, and Evaluation of Potent, Selective, and Bioavailable AKT
954 Kinase Degradation. *J. Med. Chem.* **64**, 18054–18081 (2021).
- 955 20. You, *et al.* Discovery of an AKT Degradation with Prolonged Inhibition of Downstream
956 Signaling. *Cell Chem. Biol.* **27**, 66-73.e7 (2020).
- 957 21. Zhu, *et al.* Structure-based rational design enables efficient discovery of a new selective
958 and potent AKT PROTAC degradation. *Eur. J. Med. Chem.* **238**, 114459 (2022).
- 959 22. Bricelj, *et al.* E3 Ligase Ligands in Successful PROTACs: An Overview of Syntheses and
960 Linker Attachment Points. *Front. Chem.* **9**, 1–46 (2021).
- 961 23. Liberzon, *et al.* The Molecular Signatures Database Hallmark Gene Set Collection. *Cell*
962 *Syst.* **1**, 417–425 (2015).

- 963 24. Garcia-Alonso, *et al.* Transcription factor activities enhance markers of drug sensitivity in
964 cancer. *Cancer Res.* **78**, 769–780 (2018).
- 965 25. Mahat, *et al.* Base-pair-resolution genome-wide mapping of active RNA polymerases
966 using precision nuclear run-on (PRO-seq). *Nat. Protoc.* **11**, 1455–1476 (2016).
- 967 26. Shimano, *et al.* SREBP-regulated lipid metabolism: convergent physiology — divergent
968 pathophysiology. *Nat. Rev. Endocrinol.* **13**, 710–730 (2017).
- 969 27. Goedeke, *et al.* MMAB promotes negative feedback control of cholesterol homeostasis.
970 *Nat. Commun.* **12**, (2021).
- 971 28. Chandler, *et al.* Genetic and genomic systems to study methylmalonic acidemia. *Mol.*
972 *Genet. Metab.* **86**, 34–43 (2005).
- 973 29. Dugourd, *et al.* Causal integration of multi-omics data with prior knowledge to generate
974 mechanistic hypotheses. *Mol. Syst. Biol.* **17**, 1–17 (2021).
- 975 30. Liu, *et al.* From expression footprints to causal pathways: contextualizing large signaling
976 networks with CARNIVAL. *Syst. Biol. Appl.* **5**, (2019).
- 977 31. Barabási, *et al.* Network medicine: a network-based approach to human disease. *Nat.*
978 *Rev. Genet.* **12**, 56–68 (2011).
- 979 32. Carracedo, *et al.* Inhibition of mTORC1 leads to MAPK pathway activation through a
980 PI3K-dependent feedback loop in human cancer. *J. Clin. Invest.* **118**, 3065–3074 (2008).
- 981 33. Zmajkovicova, *et al.* MEK1 Is Required for PTEN Membrane Recruitment, AKT
982 Regulation, and the Maintenance of Peripheral Tolerance. *Mol. Cell* **50**, 43–55 (2013).
- 983 34. Phong, *et al.* p38 Mitogen-Activated Protein Kinase Promotes Cell Survival in Response
984 to DNA Damage but Is Not Required for the G₂ DNA Damage Checkpoint in Human
985 Cancer Cells. *Mol. Cell. Biol.* **30**, 3816–3826 (2010).
- 986 35. Angel, *et al.* The jun proto-oncogene is positively autoregulated by its product, Jun/AP-1.
987 *Cell* **55**, 875–885 (1988).
- 988 36. Brooks, *et al.* Applicability of drug response metrics for cancer studies using biomaterials.

- 989 *Philos. Trans. R. Soc. B Biol. Sci.* **374**, (2019).
- 990 37. Tsherniak, *et al.* Defining a Cancer Dependency Map. *Cell* **170**, 564-576.e16 (2017).
- 991 38. Nusinow, *et al.* Quantitative Proteomics of the Cancer Cell Line Encyclopedia. *Cell* **180**,
992 387-402.e16 (2020).
- 993 39. Jansen, *et al.* Is there a future for AKT inhibitors in the treatment of cancer? *Clin. Cancer*
994 *Res.* **22**, 2599–2601 (2016).
- 995 40. André, *et al.* Alpelisib for PIK3CA-mutated, hormone receptor-positive advanced breast
996 cancer. *N. Engl. J. Med.* **380**, 1929–1940 (2019).
- 997 41. Madsen, *et al.* Cancer-Associated PIK3CA Mutations in Overgrowth Disorders. *Trends in*
998 *Molecular Medicine* vol. 24 856–870 (Trends Mol Med, 2018).
- 999 42. Madsen, *et al.* PIK3CA-related overgrowth: silver bullets from the cancer arsenal? *Trends*
1000 *Mol. Med.* **xx**, 1–3 (2022).
- 1001 43. Song, *et al.* RTK-Dependent Inducible Degradation of Mutant PI3K α Drives GDC-0077
1002 (Inavolisib) Efficacy. *Cancer Discov.* **0077**, (2021).
- 1003 44. Vanhaesebroeck, *et al.* Precision Targeting of Mutant PI3K α in Cancer by Selective
1004 Degradation. *Cancer Discov.* **12**, 20–22 (2022).
- 1005 45. Zhou, *et al.* Ribosomal proteins: Functions beyond the ribosome. *J. Mol. Cell Biol.* **7**, 92–
1006 104 (2015).
- 1007 46. Warner. In the absence of ribosomal RNA synthesis, the ribosomal proteins of HeLa Cells
1008 are synthesized normally and degraded rapidly. *J. Mol. Biol.* **115**, 315–333 (1977).
- 1009 47. Calleros, *et al.* RhoA and p38 MAPK mediate apoptosis induced by cellular cholesterol
1010 depletion. *Apoptosis* **11**, 1161–1173 (2006).
- 1011 48. Calleros, *et al.* Low cell cholesterol levels increase NF κ B activity through a p38 MAPK-
1012 dependent mechanism. *Cell. Signal.* **18**, 2292–2301 (2006).
- 1013 49. Donovan, *et al.* Thalidomide promotes degradation of SALL4, a transcription factor
1014 implicated in Duane radial ray syndrome. *Elife* **7**, (2018).

- 1015 50. McAlister, *et al.* MultiNotch MS3 Enables Accurate, Sensitive, and Multiplexed Detection
1016 of Differential Expression across Cancer Cell Line Proteomes. *Anal. Chem.* **86**, 7150–
1017 7158 (2014).
- 1018 51. R Core Team. *R: A language and environment for statistical computing*. R Foundation for
1019 *Statistical Computing* (2019).
- 1020 52. Ewels, *et al.* The nf-core framework for community-curated bioinformatics pipelines. *Nat.*
1021 *Biotechnol.* *2020* **383** **38**, 276–278 (2020).
- 1022 53. Dobin, *et al.* STAR: Ultrafast universal RNA-seq aligner. *Bioinformatics* **29**, 15–21 (2013).
- 1023 54. Liao, *et al.* FeatureCounts: An efficient general purpose program for assigning sequence
1024 reads to genomic features. *Bioinformatics* **30**, 923–930 (2014).
- 1025 55. Ritchie, *et al.* limma powers differential expression analyses for RNA-sequencing and
1026 microarray studies. *Nucleic Acids Res.* **43**, e47–e47 (2015).
- 1027 56. Robinson, *et al.* A scaling normalization method for differential expression analysis of
1028 RNA-seq data. *Genome Biol.* **11**, 1–9 (2010).
- 1029 57. Benjamini, *et al.* Controlling the False Discovery Rate - a Practical and Powerful
1030 Approach to Multiple Testing. *J. R. Stat. Soc. Ser. B-Methodological* **57**, 289–300 (1995).
- 1031 58. Durinck, *et al.* BioMart and Bioconductor: A powerful link between biological databases
1032 and microarray data analysis. *Bioinformatics* **21**, 3439–3440 (2005).
- 1033 59. Gu, *et al.* Complex heatmaps reveal patterns and correlations in multidimensional
1034 genomic data. *Bioinformatics* **32**, 2847–2849 (2016).
- 1035 60. Sergushichev. An algorithm for fast preranked gene set enrichment analysis using
1036 cumulative statistic calculation. *bioRxiv* 060012 (2016).
- 1037 61. Reimer, *et al.* Co-transcriptional splicing regulates 3' end cleavage during mammalian
1038 erythropoiesis. *Mol. Cell* **81**, 998-1012.e7 (2021).
- 1039 62. Szöcs, *et al.* Webchem: An R package to retrieve chemical information from the web. *J.*
1040 *Stat. Softw.* **93**, (2020).

- 1041 63. Gustavsen, *et al.* RCy3: Network biology using Cytoscape from within R. *F1000Research*
1042 **8**, 1774 (2019).
- 1043 64. Cline, *et al.* Integration of biological networks and gene expression data using cytoscape.
1044 *Nat. Protoc.* **2**, 2366–2382 (2007).
- 1045 65. Mounir, *et al.* New functionalities in the TCGAbiolinks package for the study and
1046 integration of cancer data from GDC and GTEX. *PLoS Comput. Biol.* **15**, (2019).
- 1047 66. Ho, *et al.* Moving beyond P values: data analysis with estimation graphics. *Nat. Methods*
1048 **16**, 565–566 (2019).
- 1049 67. Hafner, *et al.* Growth rate inhibition metrics correct for confounders in measuring
1050 sensitivity to cancer drugs. *Nat. Methods* **13**, 521–527 (2016).
- 1051
- 1052

1053 **Acknowledgments:** We thank members of the Toker laboratory, Joan Brugge (Harvard
1054 Medical School), Steve Elledge (Harvard Medical School), Kevin Haigis (Dana Farber Cancer
1055 Institute), Taru Muranen (Harvard Medical School), Philip Cole (Harvard Medical School), and
1056 Benjamin Turk (Yale School of Medicine), for helpful advice and suggestions; John Asara and
1057 Min Yuan for technical support with metabolomics. We would also like to thank Karen Adelman,
1058 Seth Goldman, and the Nascent transcriptomics Core (Harvard Medical School) for assistance
1059 with PRO-Seq library construction and data analysis. This work was conducted with support
1060 from Harvard Catalyst | The Harvard Clinical and Translational Science Center (National Center
1061 for Research Resources and the National Center for Advancing Translational Sciences,
1062 National Institutes of Health Award UL1 TR002541 and financial contributions from Harvard
1063 University and its affiliated academic health care centers. The content is solely the responsibility
1064 of the authors and does not necessarily represent the official views of Harvard Catalyst, Harvard
1065 University and its affiliated academic health care centers, or the National Institutes of Health.

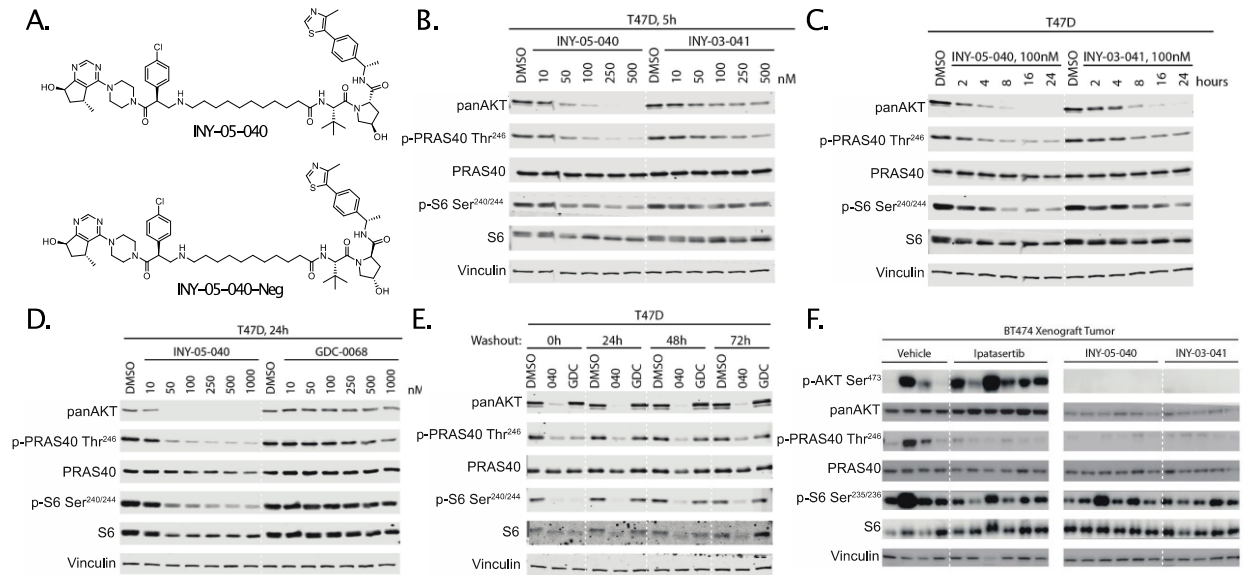
1066 **Funding:** Research support was derived in part from NIH (R35 CA253097, A. T.), and the
1067 Ludwig Center at Harvard (A.T.). E.C.E. was supported by a F31 predoctoral fellowship
1068 (5F31CA254000-02). R.R.M. was supported by a Sir Henry Wellcome Fellowship
1069 (220464/Z/20/Z). This work was supported in part by the NIH (R01 CA218278, E.S.F. and
1070 N.S.G.) N.S.G., I.Y. and E.S.F. were supported by NIH grant (5 R01 CA218278-03). **Author**
1071 **contributions:** A.T. and N.S.G. conceived the concept of AKT degraders and supervised the
1072 project. R.R.M. analyzed omics datasets, performed COSMOS, and supervised the project. I.Y.
1073 designed and synthesized the compounds and conducted experiments required for their initial
1074 chemical and biological characterization. E.C.E. designed and performed all other cell culture-
1075 based experiments. G.P. provided technical assistance. A.D. Assisted with the COSMOS
1076 installation and subsequent result interpretation. K.A.D. performed proteomics experiments
1077 under the supervision of E.S.F. J.W.J. and S.T.B. contributed to the design of studies and
1078 supervised work performed within AstraZeneca. R.E.Z. contributed to the synthesis of INY-05-

1079 040. C.C. supervised the cell panel profiling and analyzed the raw data. S.W. and J.I.M.
1080 performed xenograft experiments. S.R. performed pharmacodynamics profiling and contributed
1081 technical assistance. E.C.E., R.R.M. and A.T. wrote the manuscript and prepared figures for
1082 publication. All authors reviewed the final manuscript. **Competing interests:** K.A.D is a
1083 consultant to Kronos Bio and Neomorph Inc. E.S.F. is a founder, member of the scientific
1084 advisory board (SAB), and equity holder of Civetta Therapeutics, Proximity Therapeutics, and
1085 Neomorph Inc (also board of directors), science advisory board (SAB) member and equity
1086 holder in Avilar Therapeutics and Photys Therapeutics equity holder in Lighthouse Therapeutics,
1087 and a consultant to Astellas, Sanofi, Novartis, Deerfield, EcoR1 capital, Odyssey and Ajax
1088 Therapeutics. The Fischer laboratory receives or has received research funding from Novartis,
1089 Deerfield, Ajax, Interline, and Astellas. N.S.G. is a founder, SAB member and equity holder in
1090 Syros, C4, Allorion, Lighthouse, Voronoi, Inception, Matchpoint, CobroVentures, GSK, Larkspur
1091 (board member) and Soltego (board member). The Gray lab receives or has received research
1092 funding from Novartis, Takeda, Astellas, Taiho, Jansen, Kinogen, Arbella, Deerfield,
1093 Springworks, Interline and Sanofi. S.R., J.I.M., R.E.Z., S.W., C.C., J.W.J., and S.T.B. are
1094 employees and shareholders of AstraZeneca. **Data and materials availability:** Transcriptomic
1095 data from the RNAseq and PRO-seq analyses have been deposited with GEO under series
1096 accession number GSE206389. Proteomics data have been deposited under PRIDE accession
1097 number PXD036614. Additional source data are available at the OSF project website
1098 (<https://osf.io/3ay2w/>) with the following subcomponents: RNAseq and metabolomics raw and
1099 processed data (<https://osf.io/3f2m5/>); PROseq raw and processed data (<https://osf.io/3f2m5/>);
1100 raw and processed data for CellToxGreen-based cytotoxicity assays (<https://osf.io/fasqp/>); raw
1101 and processed data from the cell line screen and detailed protocol information, cell line-specific
1102 culture conditions and individual GI50 curve fits (<https://osf.io/us45v/>); and raw Western blot
1103 images (<https://osf.io/maq7k/>). Custom code for implementing COSMOS is available on Zenodo
1104 (doi: 10.5281/zenodo.10510991). All other data needed to evaluate the conclusions in the paper

1105 are present in the paper or the Supplementary Materials. Any outstanding information regarding
1106 the computational work will be provided by R.R.M. upon request. All custom reagents are
1107 available from A.T. and N.G. under a material transfer agreement with Harvard Medical School.

1108
1109

Figure legends



1110
1111
1112

Figure 1. Design and characterization of INY-05-040. (A) Chemical structures of INY-05-040

1113

and the negative control compound INY-05-040-Neg. (B) Immunoblots for pan-AKT, phospho-

1114

PRAS40 (Thr²⁴⁶), total PRAS40, phospho-S6 (Ser^{240/244}), total S6, and vinculin in T47D cells

1115

treated for 5 h with INY-05-040 or INY-03-041 at the indicated concentrations. Data are from a

1116

single experiment. (C) Immunoblots for pan-AKT, phospho-PRAS40 (Thr²⁴⁶), total PRAS40,

1117

phospho-S6 (Ser^{240/244}), total S6, and vinculin in T47D cells treated with INY-05-040 (100 nM) or

1118

INY-03-041 (100 nM) for the indicated times. Data are from a single experiment. (D)

1119

Immunoblots for pan-AKT, phospho-PRAS40 (Thr²⁴⁶), total PRAS40, phospho-S6 (Ser^{240/244}),

1120

total S6, and vinculin in T47D cells treated with INY-05-040 or GDC-0068 at the indicated

1121

concentrations for 24 hours. Data are from a single experiment. (E) Immunoblots for pan-AKT,

1122

phospho-PRAS40 (Thr²⁴⁶), total PRAS40, phospho-S6 (Ser^{240/244}), total S6, and vinculin in T47D

1123

cells treated with INY-05-040 (100 nM) or GDC-0068 (100 nM) for 5 h followed by washout for

1124

the indicated times. Data are from a single experiment. (F) Immunoblots for pan-AKT, phospho-

1125

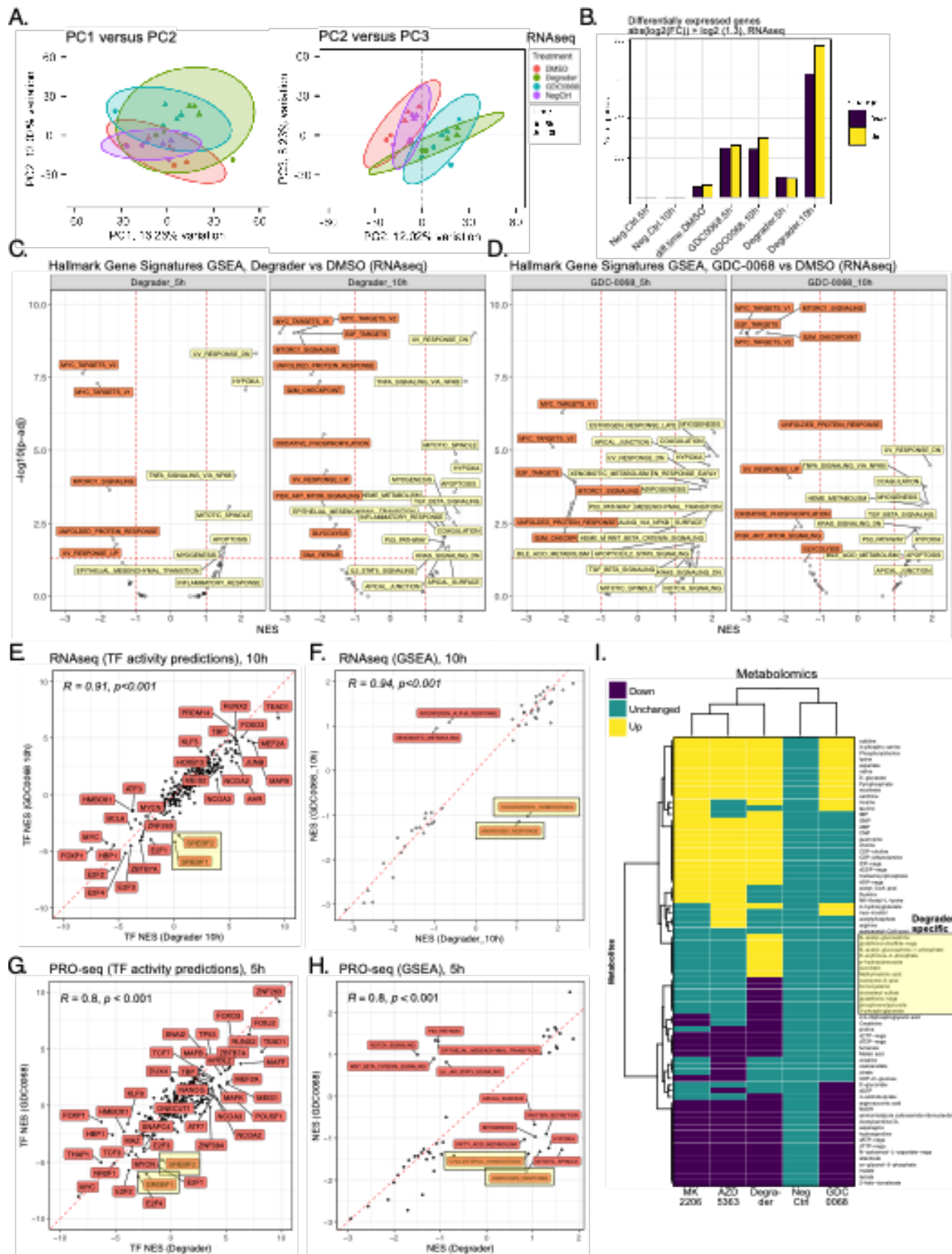
PRAS40 (Thr²⁴⁶), total PRAS40, phospho-S6 (Ser^{235/236}), total S6, and vinculin in BT-474 mouse

1126

xenograft tumors treated with vehicle (10% DMSO, 25% kleptose), GDC-0068 (12.5 mg/kg),

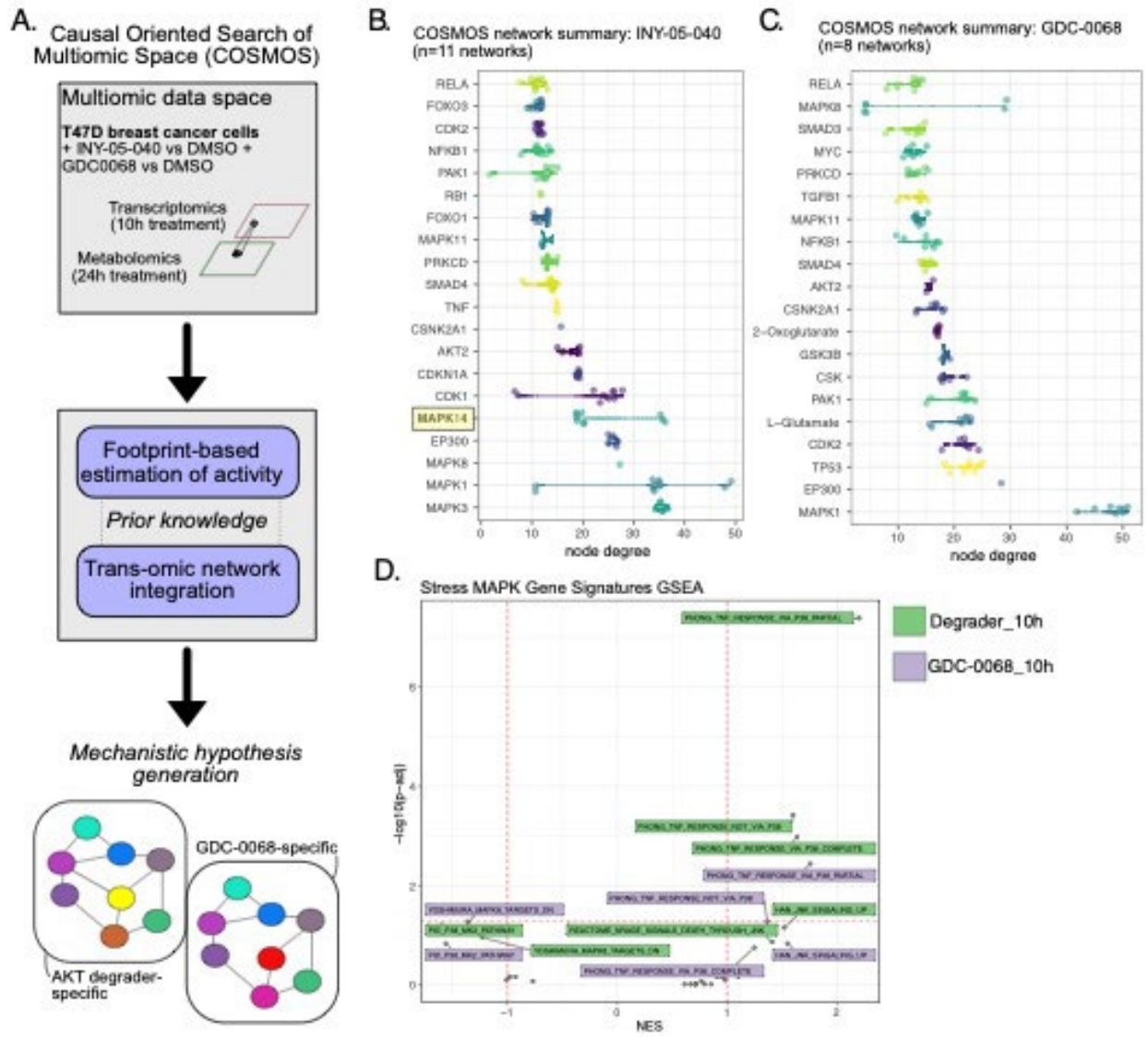
1127 INY-05-040 (25 mg/kg), or INY-03-041 (25 mg/kg) for 3 days, with a terminal treatment 4 h prior
1128 to protein harvest. N = 4-6 mice per group as shown. Panels are from the same membrane but
1129 have been cropped for clarity, with a solid white line denoting the location of the crop. Additional
1130 supporting data related to this figure are included in Fig. S1.

1131



1133 **Figure 2. Multiomic profiling of INY-05-040 and GDC-0068 in T47D breast cancer cells. (A)**
1134 Principal component analysis (PCA) projection of the transcriptomic dataset, comprising n=3
1135 biological replicates per treatment (DMSO; degrader: 100 nM INY-05-040; 500 nM GDC-0068;
1136 NegCtrl: 100 nM INY-05-040-Neg) and time point (5 h and 10 h). Ellipses are drawn around
1137 each group at 95 % confidence level. The first three independent axes (PCs) of highest variation
1138 are shown. **(B)** Number of differentially up- and downregulated transcripts (absolute fold-change
1139 ≥ 1.3) following differential gene expression analysis (FDR ≤ 0.05) across the indicated
1140 comparisons. Comparisons are relative to the corresponding DMSO-treated control; for
1141 example, Neg.Ctrl.10h refers to the effect of 10 h treatment with INY-05-040-Neg vs 10 h
1142 treatment with DMSO. The exception is “diff.time.DMSO” which evaluates differential expression
1143 as a function of time in culture (treatment with DMSO for 10 h versus treatment with DMSO for 5
1144 h). **(C and D)** Gene set enrichment analysis (GSEA) on the mSigDb HALLMARK collection,
1145 based on the ranked *t* values from all genes for the indicated treatments relative to the
1146 corresponding DMSO-treated controls. Gene sets are labelled if the absolute normalized
1147 enrichment score (NES) exceeds 1 and the adjusted p-value falls below 0.05 (FDR). **(E)**
1148 Spearman’s correlation analysis of transcription factor (TF) activity predictions from RNAseq
1149 data in cells treated for 10 h with either degrader or GDC-0068. TF footprint analyses were
1150 performed with DoRotheA. SREBF1 (protein name: SREBP1) and SREBF2 (protein name:
1151 SREBP2) activity predictions are highlighted due to their divergence between degrader and
1152 GDC-0068-treated cells, with lower activity predictions observed only in GDC-0068-treated
1153 cells. **(F)** Spearman’s correlation analysis of GSEA-derived NES for individual HALLMARK gene
1154 sets, based on RNAseq data from cells treated for 10 h with either degrader or GDC-0068.
1155 “CHOLESTEROL HOMEOSTASIS” and “ANDROGEN RESPONSE” hallmark gene sets are
1156 highlighted as having positive and negative NES in Degradere- and GDC-0068-treated cells,
1157 respectively. **(G)** Spearman’s correlation analysis of transcription factor (TF) activity predictions
1158 from PRO-seq data in T47D cells treated for 5 hours with either degrader and GDC-0068

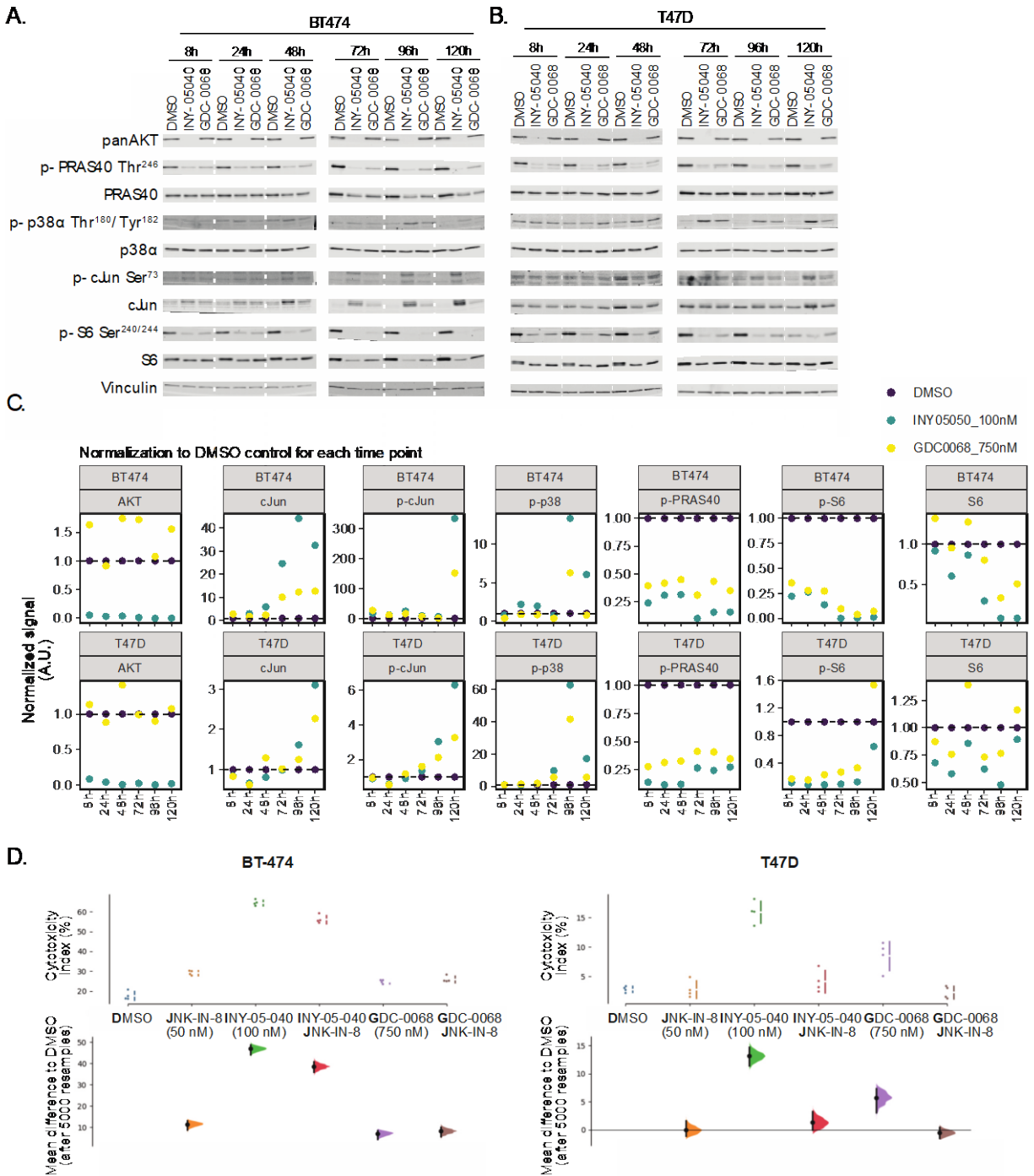
1159 relative to DMSO-treated control. TF activity predictions were calculated from *t* values from all
1160 genes following differential gene expression analysis ($FDR \leq 0.05$; $n = 2$ biological replicates
1161 per treatment). (H) Spearman's correlation analysis of GSEA-derived NES for individual
1162 HALLMARK gene sets, based on PROseq data from (G). (I) Hierarchical clustering (Euclidean
1163 distance) of differential metabolite abundance ($FDR \leq 0.05$) following 24-h treatments of T47D
1164 with either AZD 5383 (capivasertib; catalytic pan-AKT inhibitor; 2 μ M), degrader (INY-05-040;
1165 100 nM), GDC-0068 (catalytic AKT inhibitor; 500-750 nM), MK2205 (allosteric pan-AKT
1166 inhibitor; 1 μ M) or NegCtrl (INY-05-040-Neg; 100 nM). Differential abundance analysis was
1167 performed relative to DMSO-treated controls ($n = 9$ replicates per treatment, from 3 biological
1168 replicates with 3 technical replicates each). More than 85% of the observed differences in
1169 metabolite abundance for a given treatment corresponded to at least a 20% change relative to
1170 DMSO-treated cells. Metabolite levels that were changed only upon treatment with Degradar
1171 are highlighted. Additional supporting data related to this figure are included in Figs. S2, S3, S4.
1172



1173

1174 **Figure 3. COSMOS-based integration of transcriptomic and metabolomic datasets to**
 1175 **identify treatment-specific networks. (A)** Schematic illustrating the principle of COSMOS and
 1176 the datasets used for multiomic integration and predictions of treatment-specific signaling
 1177 networks. **(B and C)** Top degree nodes from degrader- and GDC-0068-specific networks plotted
 1178 in increasing order. MAPK14 (protein: p38 α) is highlighted as a degrader network-specific top
 1179 degree node. The raw COSMOS networks are included in Fig. S5 (n = 11 independent runs
 1180 using degrader data; n = 8 independent runs for GDC-0068 data). **(D)** Complementary GSEA
 1181 analyses using stress MAPK-related gene sets (mSigDb C2 collection), based on the ranked t

1182 values from all genes for the indicated treatments relative to the corresponding DMSO
1183 treatment. Gene sets are labelled if the absolute normalized enrichment score (NES) exceeds 1.
1184



1185

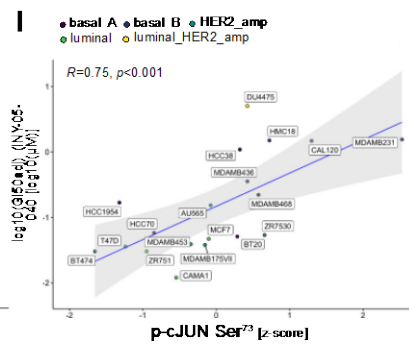
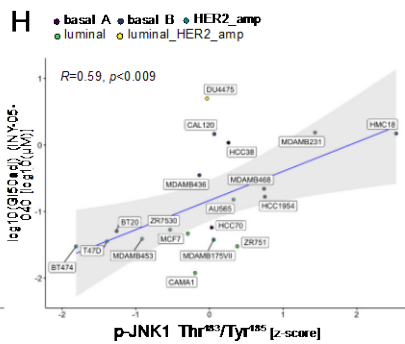
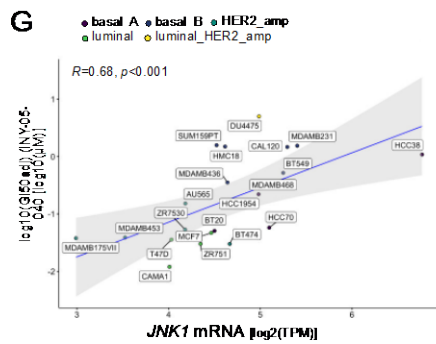
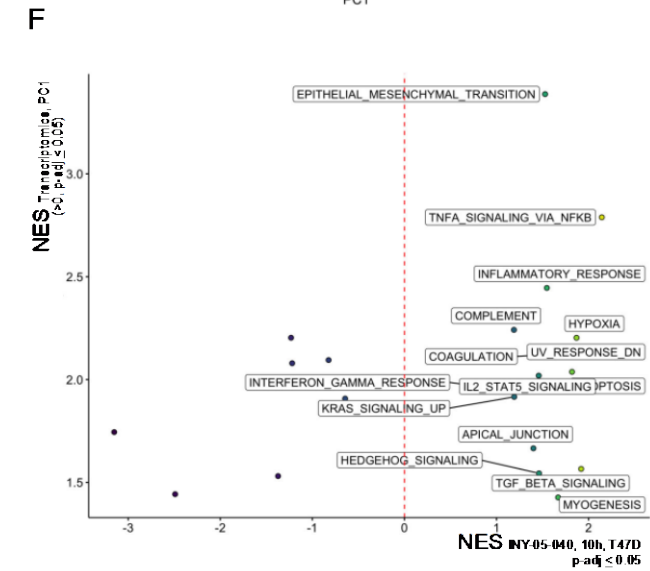
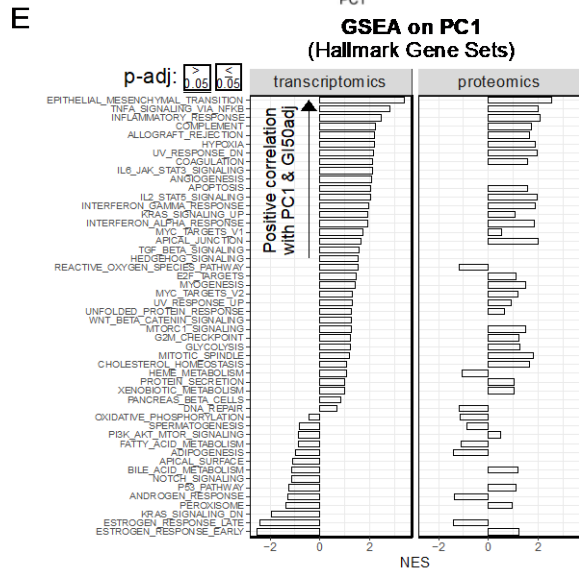
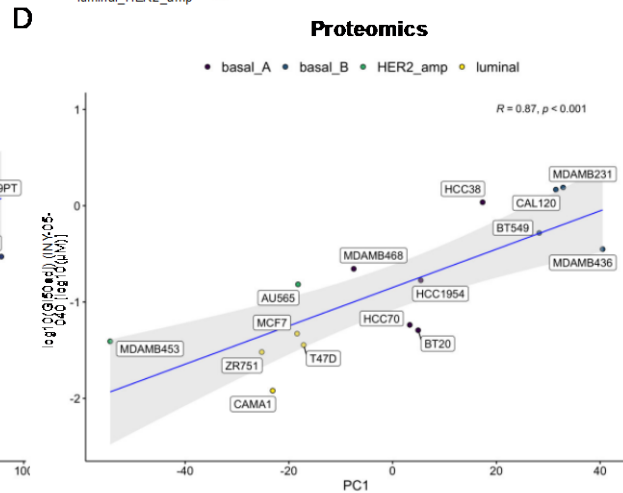
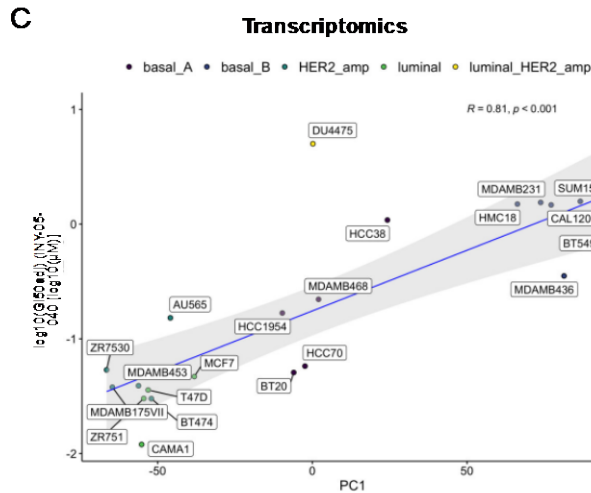
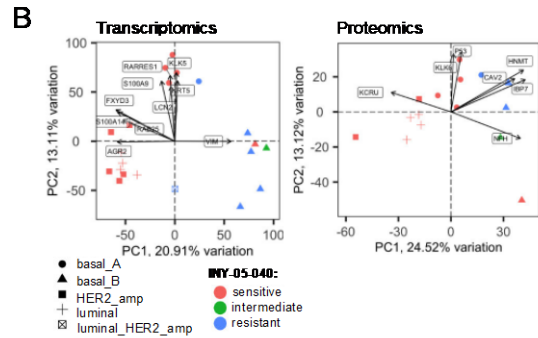
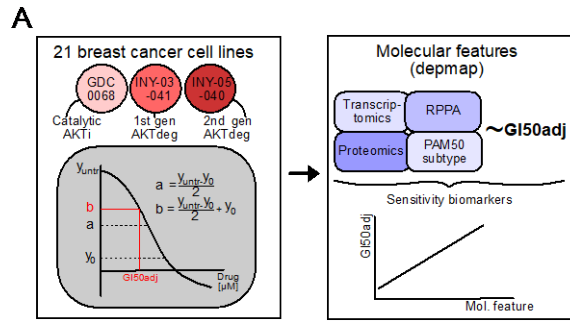
1186 **Figure 4. Validation of COSMOS-generated prediction of MAPK stress kinase signaling.**

1187 (A and B) Immunoblots for panAKT, phospho-PRAS40 (Thr²⁴⁶), total PRAS40, phospho-p38α

1188 (Thr¹⁸⁰/Tyr¹⁸²), total p38α, phospho-c-Jun (Ser⁷³), total c-Jun, phospho-S6 (Ser^{240/244}), total S6,

1189 and vinculin after treatment of BT-474 (A) or T47D (B) cells for the indicated times with DMSO,

1190 100 nM INY-05-040, or 750 nM GDC-0068. Data are from a single experiment. **(C)**
1191 Quantification of total AKT (normalized to vinculin), c-Jun (normalized to vinculin), phospho-c-
1192 Jun (pJun) Ser⁷³ (normalized to vinculin), phospho-p38 (pP38) Thr¹⁸⁰/Tyr¹⁸² (normalized to total
1193 p38), phospho-PRAS40 (pPRAS40) Thr²⁴⁶ (normalized to total PRAS40), phospho-S6 (pS6)
1194 Ser^{240/244} (normalized to vinculin) and total S6 (normalized to vinculin), including normalization to
1195 the respective DMSO control signal for each time point and cell line. Note that phospho-c-Jun
1196 and phospho-S6 were normalized to vinculin given changes in the levels of the respective total
1197 proteins. Stippled white lines are added to aid interpretation of samples loaded on the same
1198 membrane; white blocks separate samples run on different membranes. Supporting data for
1199 additional cell lines (MCF7 and MD-MB-468) are included in Fig. S6. **(C)** Cytotoxicity index
1200 assayed using CellTox Green, in BT-474 or T47D cells treated for 24 h with either DMSO or 50 nM JNK-
1201 IN-8, followed by 120-h co-treatment with either DMSO, INY-05-040 (100 nM) or GDC-0068 (750 nM). The
1202 cytotoxicity index represents cytotoxicity values corrected for background fluorescence and normalized to
1203 total signal following chemical permeabilization (used as proxy measure for total cell number). The data are
1204 displayed as Cumming plots following bootstrap-coupled estimation of effect size for each condition relative
1205 to DMSO. The upper plots display the raw data alongside standard deviations indicated with gapped
1206 lines. The plots beneath display the estimated effect sizes, sampling distribution and bootstrap 95%
1207 (percentile) confidence intervals. For accurate interpretation, please note differences in y-axis scaling. The
1208 data are from a single experiment performed with four technical replicates per condition; data from a
1209 separate experimental replicate, including a JNK-IN-8 dose curve, are in Fig. S7.
1210



1212 **Figure 5. Integration of cell line screen data with publicly available omics datasets to**
1213 **identify sensitivity biomarkers for INY-05-040. (A)** Analytical workflow for cell line screen
1214 processing and subsequent integration of the growth response metric (GI50adj) with publicly
1215 available cell line omics data from the DepMap project. A total of 288 cancer cell lines were
1216 profiled with GDC-0068, INY-03-41 and INY-05-040, with the full set of responses included in
1217 Fig. S8A. Subsequent integrative analyses focused on breast cancer cell lines only. Note that
1218 the applied growth response metric (GI50adj) takes into account cell line growth which is a
1219 known confounder in drug sensitivity measurements⁶⁷. The final output corresponds to the
1220 concentration of drug that results in 50 % cell growth inhibition. **(B)** PCA on breast cancer-
1221 specific transcriptomics and proteomics data, with coloring according to sensitivity to INY-05-
1222 040 (sensitive: $GI50adj < 0.5 \mu M$; intermediate: $0.5 \mu M \leq GI50adj \leq 1 \mu M$; resistant: $GI50adj > 1$
1223 μM ; see also Fig. S8B). The PAM50 subtype of each cell line is specified by shape. Transcripts
1224 and proteins contributing the most to the observed data structure alongside PC1 and PC2 are
1225 labelled. **(C and D)** Spearman's correlation analysis of PC1 values for each cell line and the
1226 corresponding GI50adj value for INY-05-040. A linear regression line with 95% confidence
1227 intervals (shaded area) is included in each analysis, demonstrating that cell line-specific PC1
1228 scores can be used as proxy measures for INY-05-040 sensitivity (meaning the higher the PC1
1229 score, the more resistant the cell line). **(E)** GSEA (mSigDb HALLMARK gene sets) using
1230 transcript and protein loading values alongside the respective PC1, a proxy measure for
1231 sensitivity to INY-05-040; $FDR \leq 0.05$. NES: normalized enrichment score. **(F)** A plot of all gene
1232 sets that were significantly and positively enriched across PC1 loadings from the DepMap
1233 transcriptomic data, and the corresponding NES from the T47D dataset following 10 h treatment
1234 with INY-05-040 (see also Fig. 2). Highlighted gene signatures were also statistically significant
1235 ($FDR \leq 0.05$) in the T47D dataset. **(G to I)** Spearman's correlation analysis of *JNK1* mRNA
1236 expression (G), pJNK1 (T183/Y187) (H) and p-cJun (S73) with the cell line-specific GI50adj
1237 value for INY-05-040. A linear regression line with 95% confidence intervals (shaded area) is

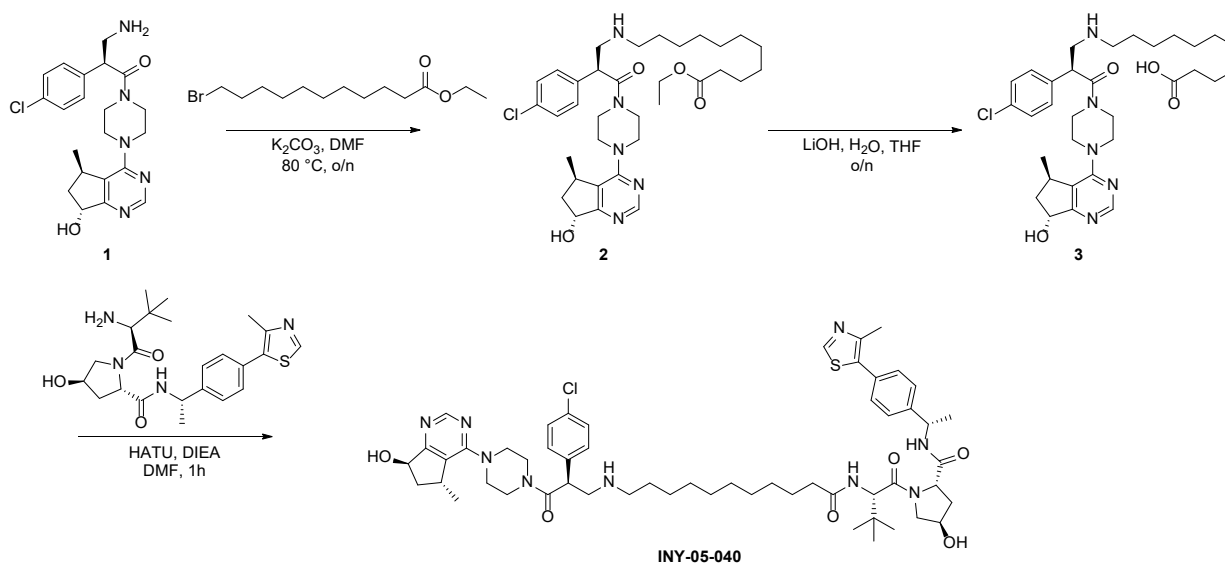
1238 included in each analysis. Reverse phase protein phosphorylation (RPPA) data were obtained
1239 from the DepMap project and subset for the signals of interest. Additional supporting data
1240 related to this figure are in Figs. S8 and S9.
1241

1242
1243
1244

Materials and Methods

Synthetic Scheme for INY-05-040

1246



1247
1248

Compound synthesis

1250 Reagents and solvents were purchased from commercial suppliers and were used
1251 without further purification unless otherwise noted. Reactions were monitored using a Waters
1252 Acquity UPLC/MS system (Waters PDA eλ Detector, QDa Detector, Sample manager – FL,
1253 Binary Solvent Manager) using Acquity HPLC® BEH C18 column (2.1 x 50 mm, 1.7 μm particle
1254 size): solvent gradient = 85% A at 0 min, 1% A at 1.7 min; solvent A = 0.1 % formic acid in
1255 water; solvent B = 0.1% formic acid in acetonitrile; flow rate: 0.6 mL/min. Products were purified
1256 by preparative HPLC using Waters SunFire™ Prep C18 column (19 x 100 mm, 5 μm particle
1257 size) using the indicated gradient in which solvent A = 0.05% trifluoroacetic acid (TFA) in water
1258 and solvent B = 0.05% TFA in methanol over 48 min (60 min run time) at a flow of 40 mL/min.
1259 ¹H NMR spectra were recorded on 500 MHz Bruker Avance III spectrometer and chemical shifts
1260 are reported in million (ppm, δ) downfield from tetramethylsilane (TMS). Coupling constants (J)

1261 are reported in Hz. Spin multiplicities are described as s (singlet), br (broad singlet), d (doublet),
1262 t (triplet), q (quartet) and m (multiplet). Purities of assayed compounds were in all cases greater
1263 than 95%, as determined by reverse-phase high-performance liquid chromatography (HPLC)
1264 analysis.

1265

1266 *Synthesis of INY-05-040 and INY-05-040-Neg*

1267

1268 Ethyl 11-(((S)-2-(4-chlorophenyl)-3-(4-((5R,7R)-7-hydroxy-5-methyl-6,7-dihydro-5H-
1269 cyclopenta[d]pyrimidin-4-yl)piperazin-1-yl)-3-oxopropyl)amino)undecanoate (2)

1270

1271 (S)-3-amino-2-(4-chlorophenyl)-1-(4-((5R,7R)-7-hydroxy-5-methyl-6,7-dihydro-5H-
1272 cyclopenta[d]pyrimidin-4-yl)piperazin-1-yl)propan-1-one (150 mg, 0.36 mmol) was dissolved in
1273 DMF (2 mL). Potassium carbonate (150 mg, 1.08 mmol) was added to the reaction mixture,
1274 then ethyl 11-bromoundecanoate (96 mg, 0.32 mmol) was added dropwise. The reaction was
1275 stirred at 80°C overnight. The next day, the reaction mixture was filtered and purified by reverse
1276 phase high-performance liquid chromatography (HPLC; 75% to 15% water in methanol) to
1277 obtain title compound as a yellow oil (133 mg, 56% yield). LC-MS: m/z 628.4 [M+1].

1278

1279 11-(((S)-2-(4-chlorophenyl)-3-(4-((5R,7R)-7-hydroxy-5-methyl-6,7-dihydro-5H-
1280 cyclopenta[d]pyrimidin-4-yl)piperazin-1-yl)-3-oxopropyl)amino)undecanoic acid (3)

1281

1282 6 N LiOH (1 mL) and THF (tetrahydrofuran; 1 mL) were added to ethyl 11-(((S)-2-(4-
1283 chlorophenyl)-3-(4-((5R,7R)-7-hydroxy-5-methyl-6,7-dihydro-5H-cyclopenta[d]pyrimidin-4-
1284 yl)piperazin-1-yl)-3-oxopropyl)amino)undecanoate (133 mg, 0.18 mmol). The reaction mixture
1285 was stirred overnight. The next day, 1 N HCl was added to pH ~3, and the solid was filtered and

1286 collected to obtain the title compound (128 mg, 99% yield) as a crude, which was used without
1287 further purification. LC-MS: m/z 600.42 [M+1].

1288

1289 (2S,4R)-1-((S)-2-(11-(((S)-2-(4-chlorophenyl)-3-(4-((5R,7R)-7-hydroxy-5-methyl-6,7-dihydro-5H-
1290 cyclopenta[d]pyrimidin-4-yl)piperazin-1-yl)-3-oxopropyl)amino)undecanamido)-3,3-
1291 dimethylbutanoyl)-4-hydroxy-N-((S)-1-(4-(4-methylthiazol-5-yl)phenyl)ethyl)pyrrolidine-2-
1292 carboxamide (INY-05-040)

1293

1294 (2S,4R)-1-((S)-2-amino-3,3-dimethylbutanoyl)-4-hydroxy-N-((S)-1-(4-(4-methylthiazol-5-
1295 yl)phenyl)ethyl)pyrrolidine-2-carboxamide (81 mg, 0.17 mmol), HATU (hexafluorophosphate
1296 azabenzotriazole tetramethyl uronium; 64 mg, 0.17 mmol), DIEA (N,N-diisopropylethylamine;
1297 200 μ L, 1.18 mmol), and DMF (dimethylformamide; 1 mL) were added to 11-(((S)-2-(4-
1298 chlorophenyl)-3-(4-((5R,7R)-7-hydroxy-5-methyl-6,7-dihydro-5H-cyclopenta[d]pyrimidin-4-
1299 yl)piperazin-1-yl)-3-oxopropyl)amino)undecanoic acid (120 mg, 0.17 mmol). The reaction was
1300 stirred for 1 h, after which the reaction was purified by reverse-phase HPLC (80% to 20% water
1301 in methanol) to obtain INY-05-040 (40 mg, 22% yield). ^1H NMR (500 MHz, DMSO) δ 9.27 (s,
1302 1H), 9.06 (s, 1H), 8.88 (s, 1H), 8.77 (s, 1H), 8.40 (d, J = 7.8 Hz, 1H), 7.78 (d, J = 9.3 Hz, 1H),
1303 7.49 – 7.43 (m, 3H), 7.41 – 7.38 (m, 3H), 5.30 (t, J = 7.9 Hz, 1H), 4.92 (p, J = 7.2 Hz, 1H), 4.75
1304 (dd, J = 8.8, 4.8 Hz, 1H), 4.52 (d, J = 9.3 Hz, 1H), 4.43 (t, J = 8.0 Hz, 1H), 4.31 – 4.25 (m, 1H),
1305 4.03 (d, J = 42.1 Hz, 2H), 3.91 – 3.78 (m, 3H), 3.72 – 3.50 (m, 6H), 3.45 – 3.33 (m, 1H), 3.08 –
1306 3.02 (m, 1H), 2.90 – 2.82 (m, 2H), 2.47 (s, 3H), 2.29 – 2.20 (m, 1H), 2.19 – 1.99 (m, 4H), 1.83 –
1307 1.76 (m, 1H), 1.67 – 1.59 (m, 2H), 1.55 – 1.40 (m, 3H), 1.38 (d, J = 7.0 Hz, 2H), 1.24 (s, 12H),
1308 1.11 (dd, J = 14.1, 6.9 Hz, 3H), 0.94 (s, 9H). LC-MS: m/z 1026.6 [M+1].

1309

1310 (2R,4S)-1-((S)-2-(11-(((S)-2-(4-chlorophenyl)-3-(4-((5R,7R)-7-hydroxy-5-methyl-6,7-dihydro-5H-
1311 cyclopenta[d]pyrimidin-4-yl)piperazin-1-yl)-3-oxopropyl)amino)undecanamido)-3,3-

1312 dimethylbutanoyl)-4-hydroxy-N-((S)-1-(4-(4-methylthiazol-5-yl)phenyl)ethyl)pyrrolidine-2-
1313 carboxamide (INY-05-040-Neg)

1314

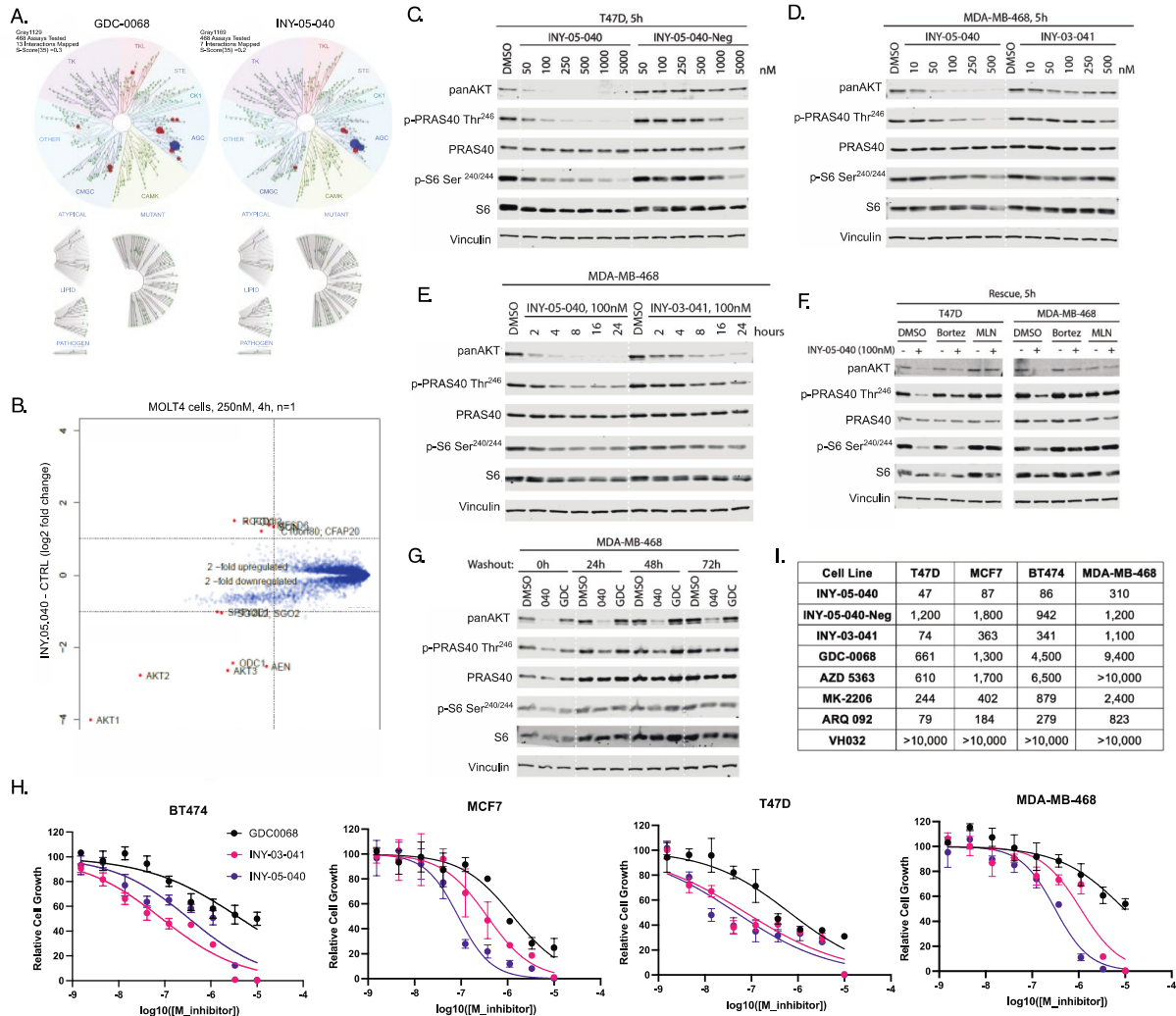
1315 INY-05-040-Neg was synthesized using similar procedures as INY-05-040 using
1316 (2R,4S)-1-((S)-2-amino-3,3-dimethylbutanoyl)-4-hydroxy-N-((S)-1-(4-(4-methylthiazol-5-
1317 yl)phenyl)ethyl)pyrrolidine-2-carboxamide as the starting material. ¹H NMR (500 MHz, DMSO) δ
1318 8.99 (s, 1H), 8.70 (s, 1H), 8.54 (s, 1H), 8.40 (s, 1H), 8.06 (d, J = 8.0 Hz, 1H), 7.89 (d, J = 7.8 Hz,
1319 1H), 7.49 (d, 2H), 7.45 – 7.44 (m, 3H), 7.38 – 7.35 (m, 2H), 5.20 (t, J = 7.6 Hz, 1H), 4.91 (p,
1320 1H), 4.48 (dd, J = 8.7, 5.0 Hz, 1H), 4.42 – 4.37 (m, 2H), 4.33 – 4.28 (m, 1H), 3.98 (s, 1H), 3.80
1321 (dd, J = 10.4, 5.4 Hz, 2H), 3.77 – 3.58 (m, 6H), 3.56 – 3.45 (m, 3H), 3.14 – 3.07 (m, 1H), 2.94 –
1322 2.86 (m, 2H), 2.47 (s, 3H), 2.29 – 2.21 (m, 1H), 2.14 – 1.93 (m, 6H), 1.62 – 1.52 (m, 2H), 1.52 –
1323 1.38 (m, 3H), 1.32 (d, J = 7.0 Hz, 3H), 1.26 – 1.17 (m, 13H), 1.08 (d, J = 6.9 Hz, 3H), 0.97 (s,
1324 9H). LC-MS: m/z 1026.57 [M+1].

1325

1326

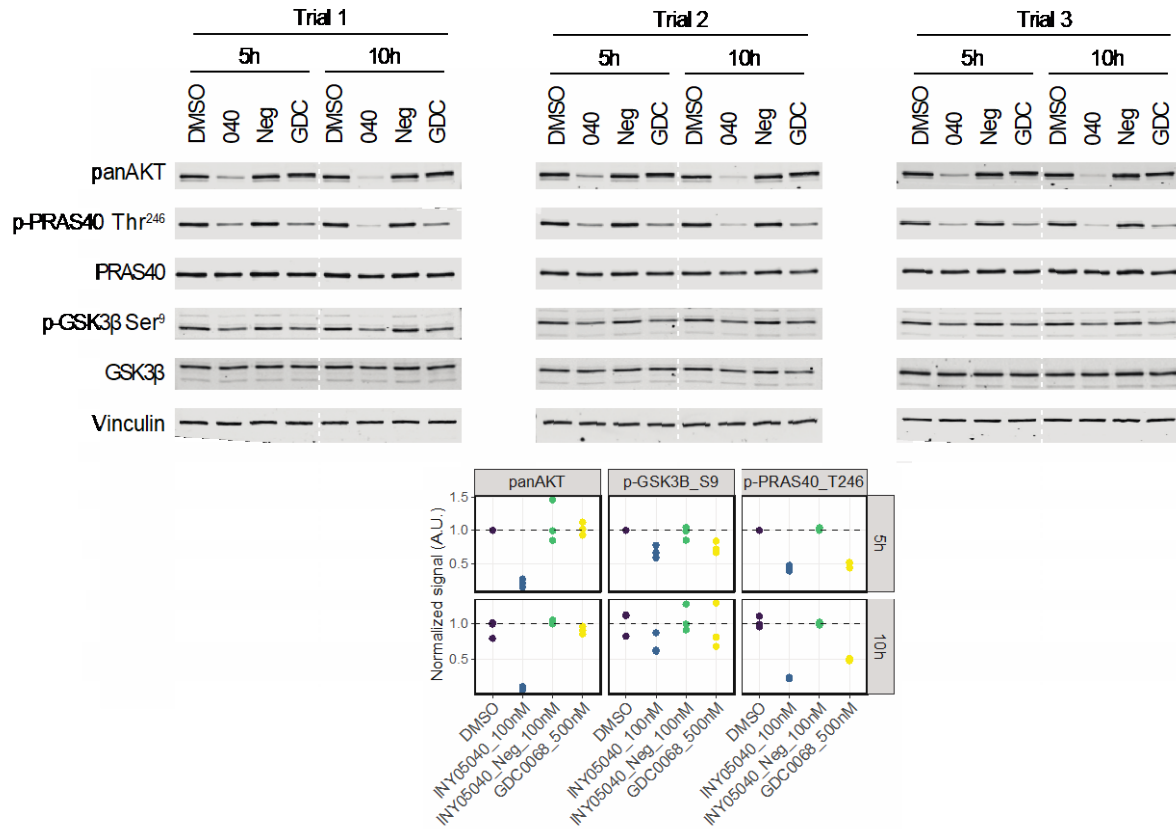
1327

1328



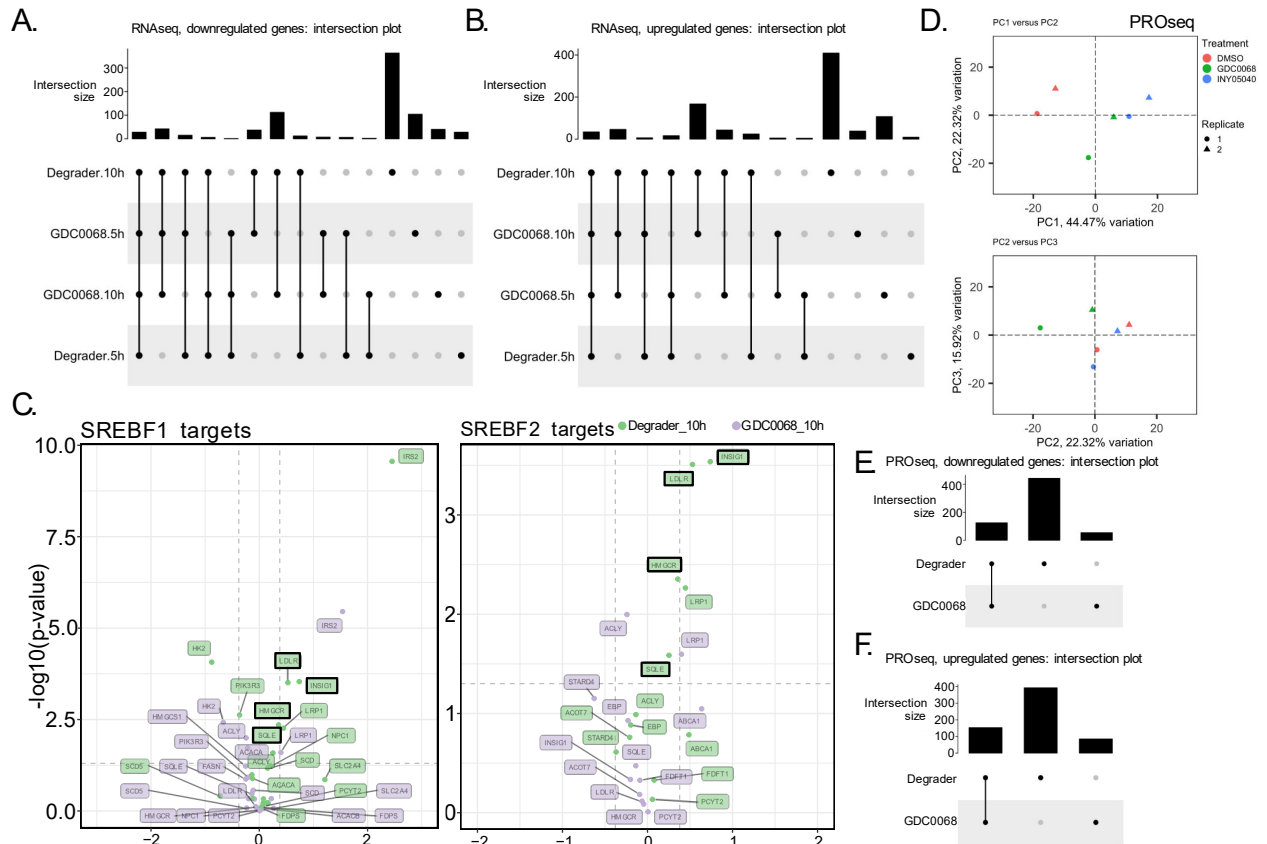
1329
 1330
 1331 **Figure S1. INY-05-040 biochemical selectivity and proteomics analysis of INY-05-040-treated cells.**
 1332 (A) TREEspot visualization of the biochemical selectivity profile of GDC-0068 and INY-05-040 (1 μ M). AKT
 1333 isoforms are highlighted in blue; all other inhibited kinases are highlighted in red. (B) Scatterplot plot of relative
 1334 protein abundance changes in MOLT4 cells treated with INY-05-040 (250 nM) compared to DMSO (vehicle)
 1335 for 4 hours, measured using tandem mass tag quantitative mass spectrometry. The log₂ fold-change (FC)
 1336 is shown on the y axis for one independent biological replicate for drug treatment and 3 independent
 1337 biological replicates for DMSO treatments. The short duration (4 hours) of the assay was chosen to capture
 1338 acute changes in protein levels that could be due to both on- and off-target effects, as opposed to secondary
 1339 on-target changes occurring upon prolonged drug treatment. (C) Immunoblots for pan-AKT, phospho-
 1340 PRAS40 (Thr²⁴⁶), total PRAS40, phospho-S6 (Ser^{240/244}), total S6, and vinculin in T47D cells treated for 5
 1341 hours with DMSO, INY-05-040 (040) or INY-05-040-Neg at the indicated doses. Data are from a single
 1342 experiment. (D) Immunoblots for the same components as in (C) but in MDA-MB-468 cells treated for 5 h
 1343 with DMSO, INY-05-040 or GDC-0068 at the indicated concentrations. Data are from a single
 1344 experiment. (E) Immunoblots for the same components as in (C), but in MDA-MB-468 cells treated with
 1345 DMSO, INY-05-040 (100 nM) or INY-03-041 (100 nM) for the indicated times. Data are from a single
 1346 experiment. (F) Immunoblots for the same components as in (C), but in T47D or MDA-MB-468 cells
 1347 cotreated for 5 hours with DMSO, bortezomib (0.5 mM), or MLN-4924 (1 mM), and either INY-05-040 (100
 1348 nM) or DMSO. Data are from a single experiment. (G) Immunoblots for the same components as in (C),
 but in MDA-MB-468 cells treated for 5 hours with DMSO, INY-05-040 (100 nM) or GDC-0068 (100 nM),

1349 followed by washout for the indicated times. Data are from a single experiment. (H) CellTiter Glo assay
1350 evaluating percent inhibition in cell growth relative to DMSO treatment in T47D, MCF7, BT-474, or MDA-
1351 MB-468 cells, treated for 72 h with INY-03-041, INY-05-040 or GDC-0068. N=2 biological replicates for
1352 MCF7 and BT474, each in technical triplicate; N=1 biological replicate for T47D and M468, each
1353 in technical triplicate. (I) Table representing cell line-specific EC50 values (nM) calculated from the
1354 respective CellTiter Glo assays in (H). Stippled white lines added to aid interpretation of samples
1355 loaded on the same membrane; white blocks separate samples run on different membranes.
1356
1357
1358
1359
1360
1361
1362



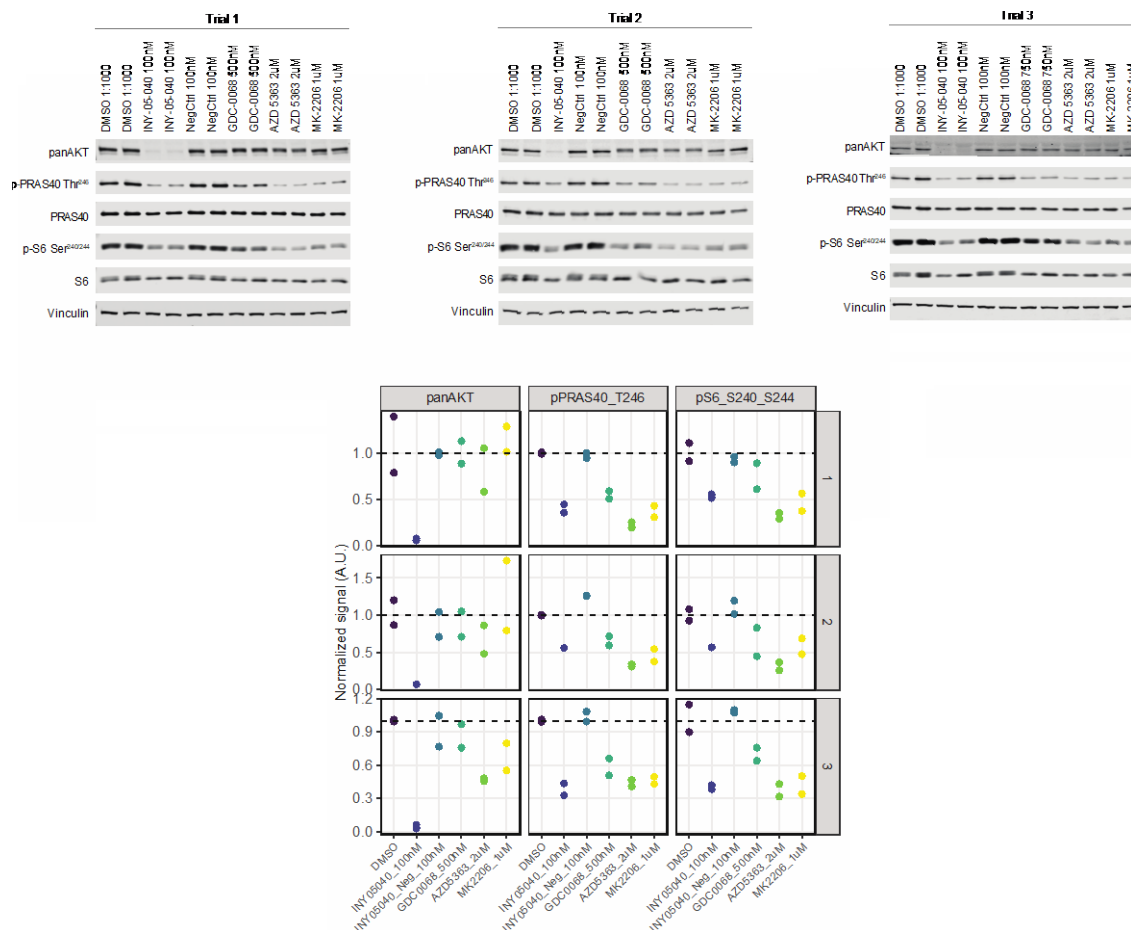
1363
 1364
 1365
 1366
 1367
 1368
 1369
 1370
 1371
 1372
 1373
 1374
 1375
 1376
 1377

Figure S2. Signaling immunoblots related to RNAseq analysis. Immunoblots and associated quantifications for pan-AKT, phospho-PRAS40 (Thr²⁴⁶), total PRAS40, phospho-GSK3β (Ser⁹), total GSK3β, phospho-S6 (Ser^{240/244}), total S6, and vinculin in T47D cells treated for 5 h or 10 h with DMSO, 100 nM INY-05-040 (O40), 100 nM INY-05-040-Neg (Neg), or 500 nM GDC-0068 (GDC), collected in parallel with the corresponding RNAseq samples. Quantification of AKT represents protein abundance over vinculin, relative to the corresponding DMSO condition for each time point. Quantification of remaining phosphorylated proteins represent normalization to the corresponding total protein, relative to the DMSO signal for each time point. Stippled white lines added to aid interpretation of samples loaded on the same membrane. N=3 biological replicates per group, with each replicate represented as a separate trial.



1379
 1380
 1381
 1382
 1383
 1384
 1385
 1386
 1387
 1388
 1389
 1390
 1391
 1392
 1393
 1394

Figure S3. Supporting multiomic data analyses of T47D breast cancer cells. (A and B) UpSet intersection plots for up- (A) and down-regulated (B) transcripts, respectively, for the indicated treatments relative to DMSO. Fold-change cut-off for differential expression was 1.3; $FDR \leq 0.05$. Only genes with HGNC (HUGO Gene Nomenclature Committee) annotation were included in the final count. **(C)** Volcano plot of SREBF1 and SREBF2 target gene expression in degrader- and GDC-0068-treated T47D cells. The horizontal dotted line indicates the adjusted p-value cut-off for statistical significance ($FDR \leq 0.05$); the vertical dotted lines specify the cut-off corresponding to a fold-change of $\log_2(1.3)$ for up- or down-regulation. The target genes correspond to those used for transcription factor footprint estimates with DoRoThEA. Black rectangles are used to highlight cholesterol synthesis genes that are selectively upregulated in Degradar- but not GDC-0068-treated cells after 10 hours. **(D)** Principal component analysis (PCA) of the PROseq dataset, comprising $n = 2$ biological replicates per treatment (all performed for 5 h). The first three independent axes (principal components; PCs) of highest variation are shown. **(E and F)** As for (A) and (B), respectively, but using differentially expressed genes from the PROseq dataset.



1395
 1396
 1397
 1398
 1399
 1400
 1401
 1402
 1403
 1404
 1405
 1406
 1407
 1408

Figure S4. Signaling immunoblots related to metabolomics. Immunoblots and associated quantifications for pan-AKT, phospho-PRAS40 (Thr²⁴⁶), total PRAS40, phospho-S6 (Ser^{240/244}), total S6, and vinculin in T47D cells treated for 24 h with DMSO, INY-05-040, INY-05-040-Neg, GDC-0068, AZD 5363, or MK-2206 as indicated; samples were collected in parallel with the corresponding metabolomics samples. Note that the dose of GDC-0068 was increased to 750 nM in Trial 3 to retain consistent levels of signaling suppression relative to the previous experiments. Quantification of AKT represents protein abundance over vinculin, relative to the average of the replicate DMSO samples. Quantification of the phosphorylated proteins represent normalization to the corresponding total protein, relative to the average of the replicate DMSO samples.

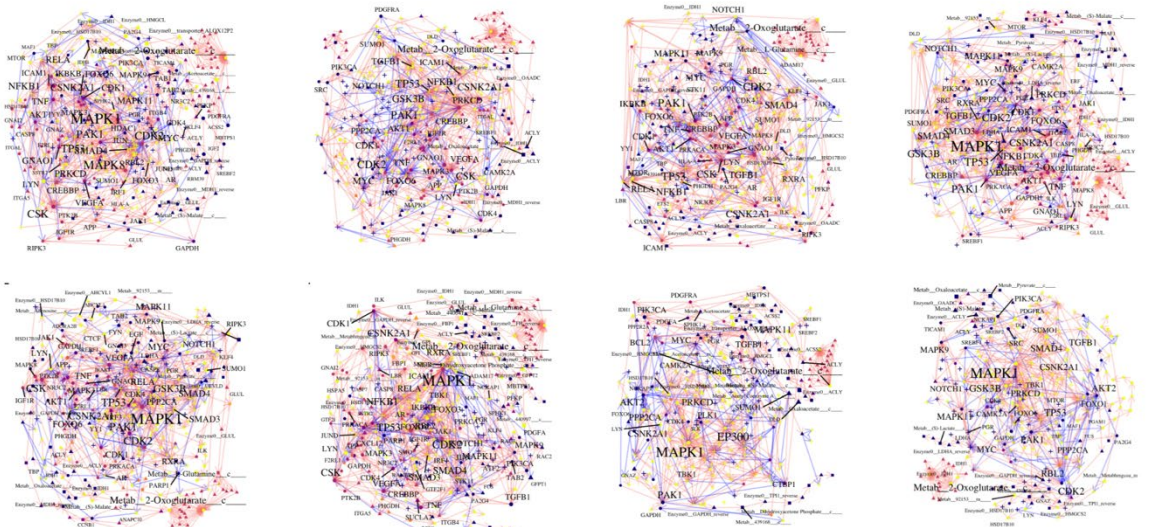
A.

COSMOS: Degradator-specific networks (T47D)



B.

COSMOS: GDC0068-specific networks (T47D)

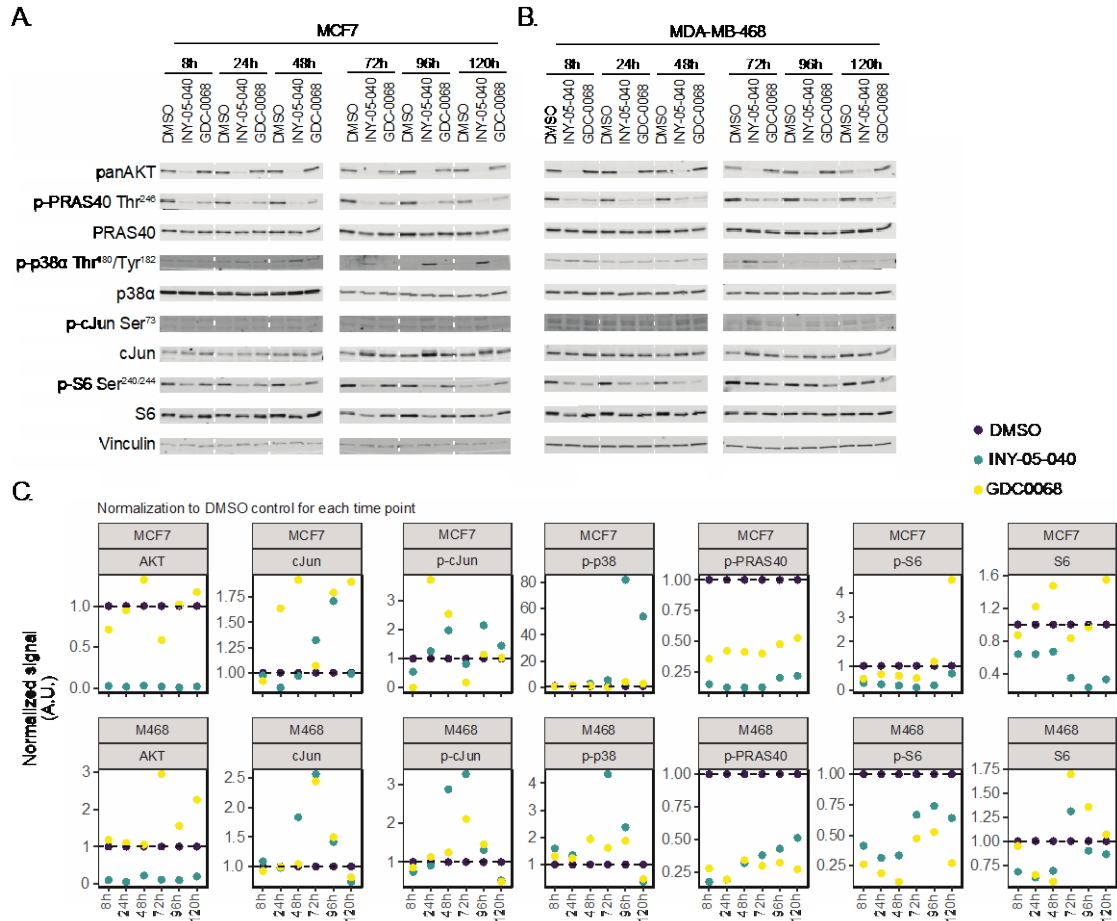


1409
1410

1411
1412
1413
1414
1415

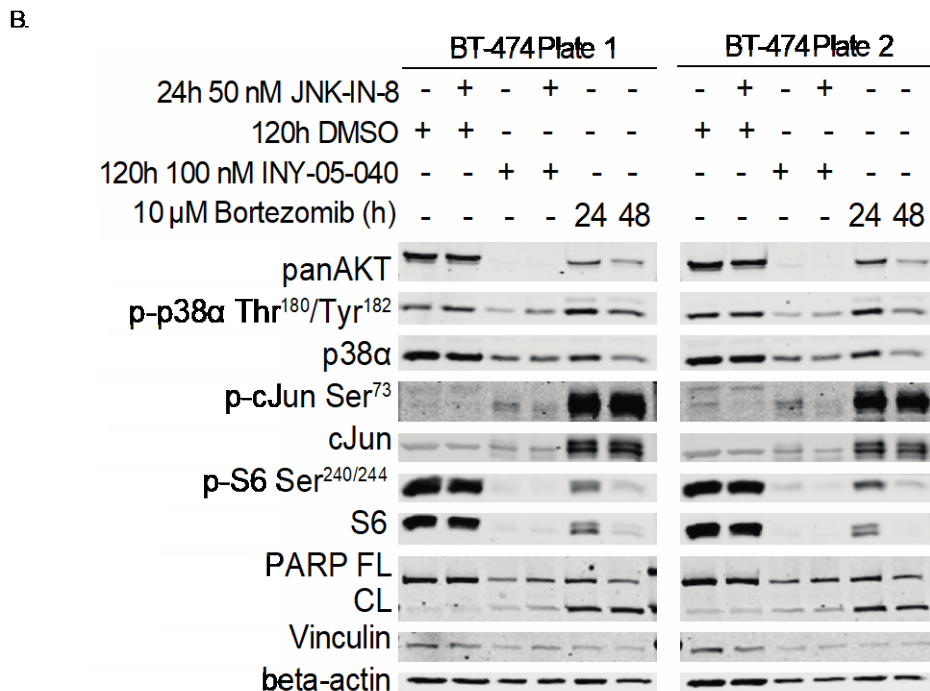
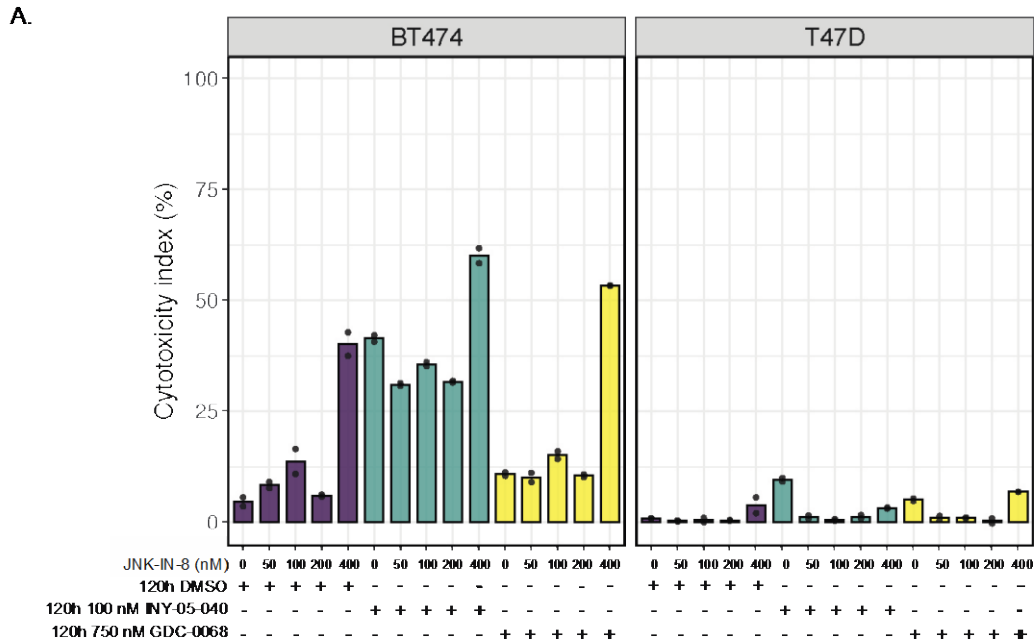
Figure S5. Individual COSMOS networks following integration of T47D transcriptomic and metabolomic data. (A and B) Networks are specific to degrader (A) and GDC-0068 (B) treatments. For details of the analytical framework, refer to Fig. 3A. Predicted inhibitory (-1) and activating (1) interactions are indicated. Predicted average node activity (AvgAct) in each network model is visualized on a scale from -1 (inhibited) to 1 (activated). Each network was generated following an independent COSMOS run with the

1416 same data but with varying settings to ensure robustness of the final output (for additional information on run-
1417 specific settings, see <https://osf.io/tdvur/>).
1418
1419



1420
1421
1422
1423
1424
1425
1426
1427
1428
1429
1430
1431
1432
1433
1434
1435

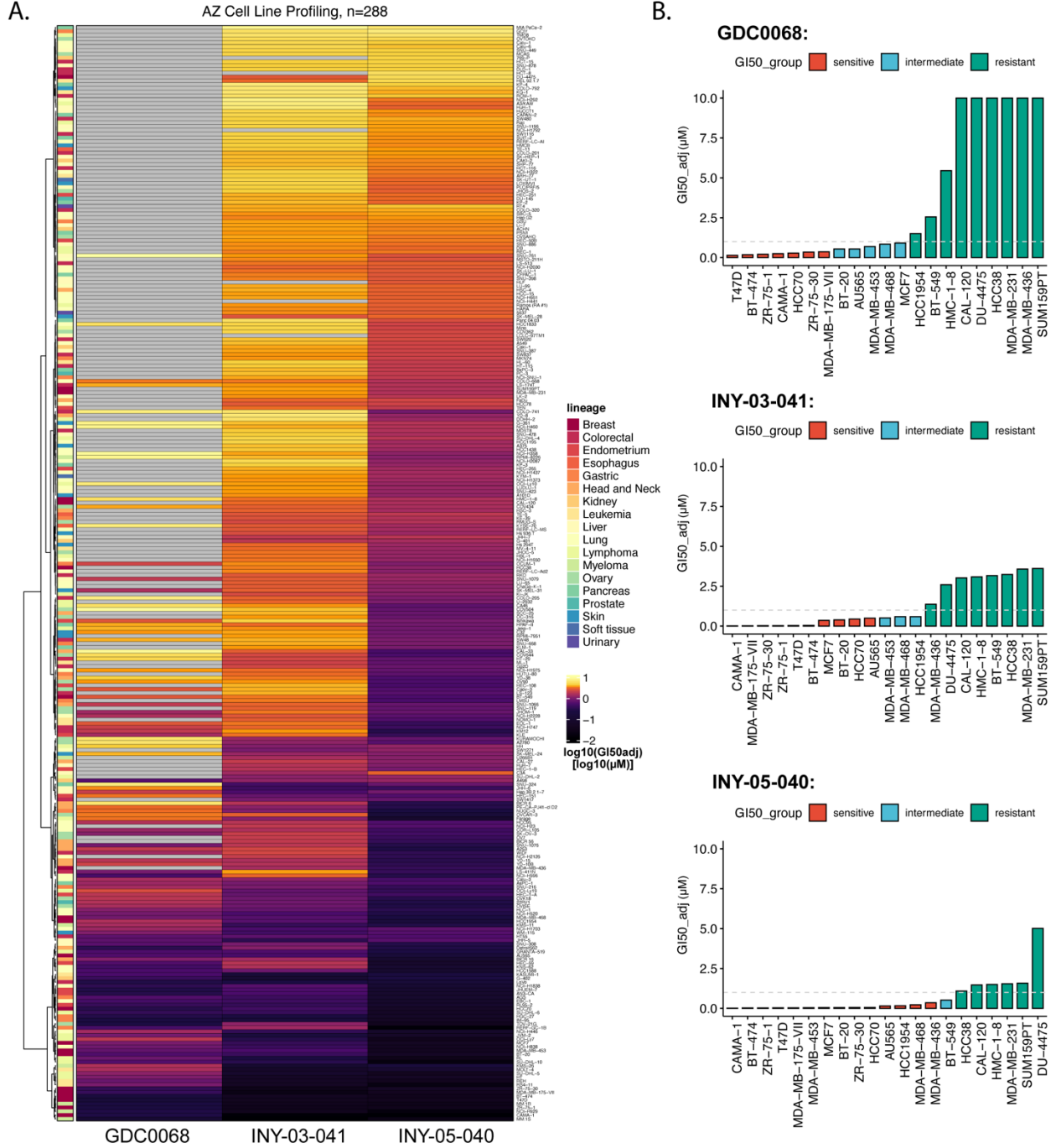
Figure S6. Stress MAPK signaling activation in MCF7 and MDA-MB-468 cells. (A and B) Immunoblots for pan-AKT, phospho-PRAS40 (Thr²⁴⁶), total PRAS40, phospho-p38α (Thr¹⁸⁰/Tyr¹⁸²), total p38α, phospho-c-Jun (Ser⁷³), total c-Jun, phospho-S6 (Ser^{240/244}), total S6, and vinculin after DMSO, INY-05-040 (100 nM) or GDC-0068 (750 nM) treatment of MCF7 (A) or MDA-MB-468 (B) cells for the indicated times. Stippled white lines are added to aid interpretation of samples loaded on the same membrane; white blocks separate samples run on different membranes. Data are from a single experiment. (C) Quantification of total AKT (normalized to vinculin), c-Jun (normalized to vinculin), phospho-c-Jun (pJun) Ser⁷³ (normalized to vinculin), phospho-p38 (pP38) Thr¹⁸⁰/Tyr¹⁸² (normalized to total p38), phospho-PRAS40 (pPRAS40) Thr²⁴⁶ (normalized to total PRAS40), phospho-S6 (pS6) Ser^{240/244} (normalized to vinculin) and total S6 (normalized to vinculin), including normalization to the respective DMSO control signal for each time point and cell line. Note that phospho-c-Jun and phospho-S6 were normalized to vinculin given changes in the levels of the respective total proteins.



1436
 1437 **Figure S7. Cell viability after pre-treatment of cells with JNK-IN-8.** (A) Cytotoxicity index, assayed using
 1438 CellTox Green, in BT-474 or T47D cells treated for 24 h with either DMSO or the indicated concentrations of
 1439 JNK-IN-8, followed by 120-h co-treatment with either DMSO, INY-05-040 (100 nM) or GDC-0068 (750 nM).
 1440 The cytotoxicity index represents cytotoxicity values corrected for background fluorescence and normalized
 1441 to total signal following chemical permeabilization (used as proxy measure for total cell number). The data
 1442 are from a single experiment with two technical replicates per treatment. Additional data replicating the key
 1443 results are shown in Figure 4D. (B) Immunoblots for pan-AKT, phospho-p38α (Thr¹⁸⁰/Tyr¹⁸²), total p38α,
 1444 phospho-c-Jun (Ser⁷³), total c-Jun, phospho-S6 (Ser^{240/244}), total S6, PARP (FL: full lengths; CL: cleaved),
 1445 vinculin, and beta-actin after 24 h pre-treatment of BT474 cells with either DMSO or 50 nM JNK-IN-8,

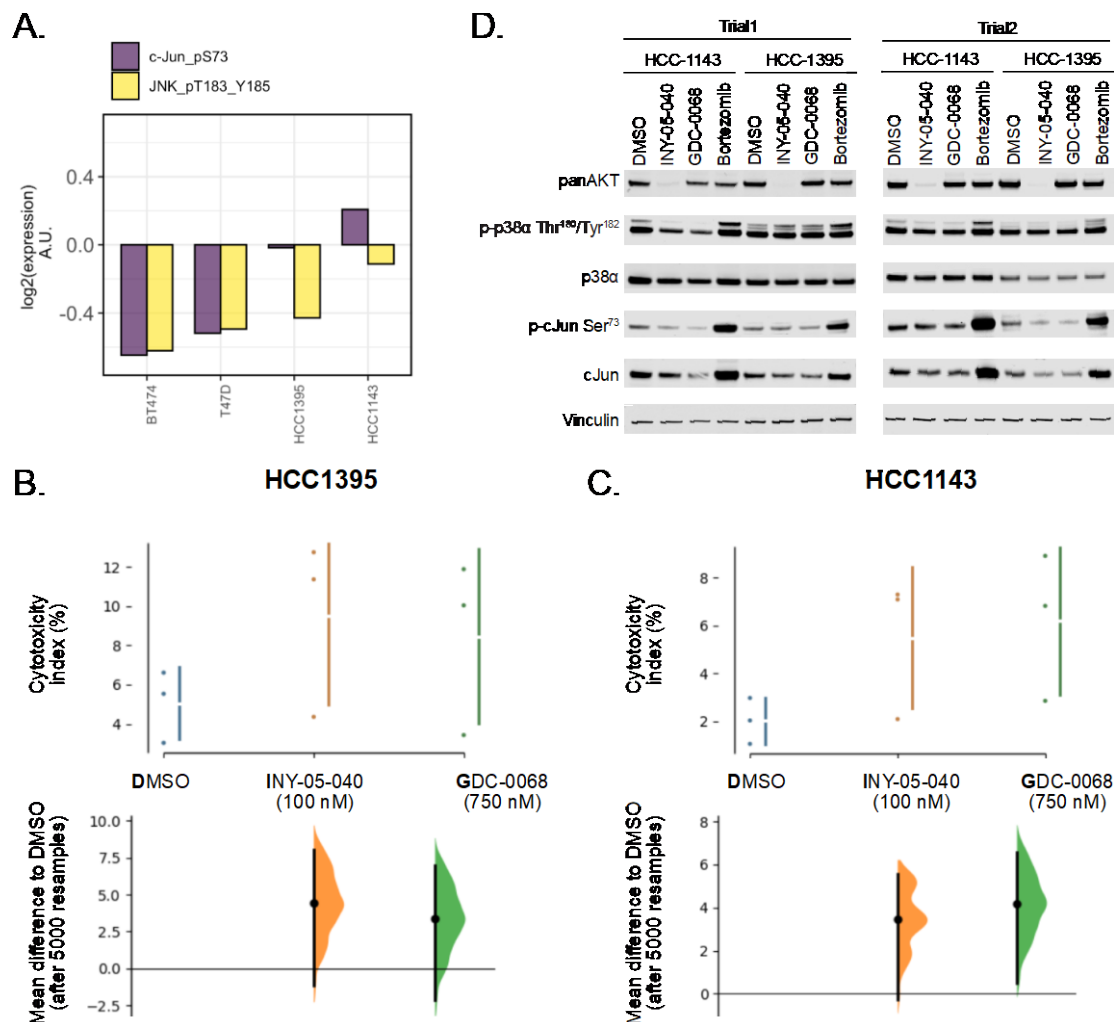
1446 followed by 120-h co-treatment with either DMSO, INY-05-040 (100 nM) or GDC-0068 (750 nM). Treatment
1447 with bortezomib (10 μ M) for 24 h and 48 h was used as positive control. Two technical replicates (Plate 1
1448 and Plate 2) were processed in parallel. Complementary brightfield microscopy images for both (A) and (B)
1449 are provided on the OSF project website (<https://osf.io/fasqp/>). Quantification for cleaved (CL) PARP was
1450 performed by measuring the intensity of the indicated lower band, normalized to beta-actin, relative to DMSO.

1451
1452



1453
1454
1455
1456
1457
1458
1459
1460
1461

Figure S8. Screen of cancer cell lines with GDC-0068, INY-03-041, and INY-05-040. (A) Heatmap of cell line-specific GI50adj values for each compound, with Euclidean distance-based clustering of the cell lines (rows). (B) Barplots indicating the GI50adj values for each compound in breast cancer cell lines only, colored according to sensitivity to the respective compound (sensitive: GI50adj < 0.5 μM; intermediate: 0.5 μM < GI50adj < 1 μM; resistant: GI50adj > 1 μM). The dotted horizontal line indicates GI50adj = 1 μM.



1462
 1463
 1464
 1465
 1466
 1467
 1468
 1469
 1470
 1471
 1472
 1473
 1474
 1475
 1476
 1477
 1478
 1479
 1480

Figure S9. Independent experimental validation of model relating JNK activity and breast cancer cell death following AKT inhibition. (A) Reverse phase protein phosphorylation (RPPA) from the DepMAP project, subset for phospho-c-Jun (Ser⁷³) and phospho-JNK1 (Thr¹⁸³, Tyr¹⁸⁵) in BT-474, T47D, HCC-1395 and HCC-1143 breast cancer cell lines in order of relative expression for the two signaling markers. Data are from a single experiment. (B and C) Cytotoxicity index assayed using CellTox Green, in HCC-1395 and HCC-1143 cells treated for 120-h with either DMSO, INY-05-040 (100 nM) or GDC-0068 (750 nM). The cytotoxicity index represents cytotoxicity values corrected for background fluorescence and normalized to total signal following chemical permeabilization (used as proxy measure for total cell number). The data are displayed as Cumming plots following bootstrap-coupled estimation of effect size for each condition relative to DMSO. The upper plots display the raw data alongside standard deviations indicated with gapped lines. The plots beneath display the estimated effect sizes, sampling distribution and bootstrap 95% (percentile) confidence intervals. For accurate interpretation, please note differences in y-axis scaling. The data are from three biological replicates per group. (D) Immunoblots for pan-AKT, phospho-p38α (Thr¹⁸⁰/Tyr¹⁸²), total p38α, phospho-c-Jun (Ser⁷³), total c-Jun, and vinculin in HCC-1143 or HCC-1395 cells treated with DMSO, INY-05-040 (100 nM), or GDC-0068 (750 nM) for 5 days or bortezomib (1 μM) for 24h. N=2 biological replicates per group.

1481 **Table S1.** Plasma concentration after the first dose of GDC-0068.
 1482

GDC-0068 12.5mg/kg PO								
Time	Plasma Concentration (μM)							
(h)	MEAN	\pm Error	10	23	26	44	72	75
0.5	2.5563	1.6733	0.5112	2.9583	1.3482	1.7964	3.6207	5.103
2.0	0.8718	0.6479	1.6011	0.6192	0.4644	0.6165	0.1728	1.7568
6.0	1.3839	0.5764	2.1654	1.1412	1.8522	1.5525	0.6336	0.9585
12.0	1.7514	0.9318	1.4526	1.3959	1.3248	1.4184	1.2681	3.6486
24.0	0.0729	0.0383	0.1278	0.0306	0.036	0.0909	0.0963	0.0558

1483 **Table S2.** Plasma concentration after the first dose of INY-05-040.
 1484
 1485

INY-05-040 25mg/kg IP								
Time	Plasma Concentration (μM)							
(h)	MEAN	\pm Error	21	25	43	45	59	63
0.5	3.0152	3.6181	0.7434	0.9756	1.0215	0.9387	9.7281	4.6836
2.0	10.1405	7.7061	13.9356	8.1279	8.0523	23.715	4.4568	2.5551
6.0	0.2263	0.0980	0.1467	0.3465	0.3399	0.2313	0.1179	0.1755
12.0	0.1995	0.0744	0.1035	0.1872	0.1503	0.1809	0.2862	0.2889
24.0	0.6363	0.1115	0.7722	0.5544	0.7794	0.5301	0.6138	0.5679

1486 **Table S3.** Plasma concentration after the first dose of INY-03-041.
 1487
 1488

INY-03-041 25mg/kg IP								
Time	Plasma Concentration (μM)							
(h)	MEAN	\pm Error	2	5	7	16	42	67
0.5	6.1394	5.1860	2.7594	2.0349	2.5425	4.1175	11.4003	13.9815
2.0	11.7695	2.3175	14.3631	9.4635	13.0887	12.1599	13.1076	8.4339
6.0	0.2798	0.2334	0.6408	0.2682	0.0558	0.0957	<0.009	0.3384
12.0	0.9876	0.4460	0.9855	1.287	1.4706	0.7992	0.2115	1.1718
24.0	0.7874	0.1256	0.7821	0.8199	0.8667	0.7668	0.9279	0.5607

1489

1490 **Table S4. Mouse body weights.** Body weights (grams) of mice proceeded to endpoint for
 1491 pharmacodynamics after treatment with 12.5 mg/kg GDC-0068 PO BID, 25 mg/kg INY-05-040 IP
 1492 QD, or 25 mg/kg INY-03-041 IP QD.
 1493

	Mouse	Days post-select			
		0	4	5	6
Vehicle	15	27	26.2	25.9	25.9
	47	34.1	33	N/A	N/A
	54	28.7	28.9	28.4	28.6
	58	30.4	30.7	N/A	N/A
	62	33.3	34.3	33.5	33.4
	68	28.1	28.6	27.9	27.5
GDC-0068 12.5 mg/kg	6	32.5	32.9	32.4	33.1
	17	28.2	27.8	27.6	28
	24	26.3	25.9	25.6	25.7
	50	34.9	35.1	35	34.8
	57	30.7	30.9	30.9	29.9
	60	28.6	29	29	28.3
INY-05-040 25 mg/kg	8	33.2	32.8	31.3	30.5
	9	28.3	28.7	26.8	26.6
	28	26.8	26.9	24.7	23.8
	52	29.5	29.2	28.5	27.8
	61	27.9	27.9	27.2	26.9
	73	32	31.8	30.2	29.5
INY-03-041 25 mg/kg	19	31.4	30.5	29.6	29.7
	29	27.9	26.9	25.6	25.7
	35	28.1	27.8	25.2	24.5
	39	31.1	32.5	30.7	30.9
	40	29.8	28.7	27.9	28.3
	64	27.6	28.5	27.6	27.4

1494
 1495 **Table S5: Primary Antibodies**

1° antibody	Mol. Weight (kDa)	Lot #	Vendor	Cat. #	RRID
pan-AKT	60	20	Cell Signaling Technology	4691	AB_915783
pan-AKT	60	Not recorded	Cell Signaling Technology	9275	AB_329828

pAKT (Ser ⁴⁷³)	60	24	Cell Signaling Technology	4060	AB_2315049
pAKT (Thr ³⁰⁸)	80	18	Cell Signaling Technology	2965	AB_2255933
pPRAS40 (Thr ²⁴⁶)	40	12	Cell Signaling Technology	2997	AB_2258110
pPRAS40	40	Not recorded	Cell Signaling Technology	13175	AB_2798140
Total PRAS40	40	11	Cell Signaling Technology	2691	AB_2225033
Total PRAS40	40	Not recorded	Cell Signaling Technology	2610	AB_916206
pGSK3 β (Ser ⁹)	46	13	Cell Signaling Technology	9336	AB_331405
GSK3 β	46	14	Cell Signaling Technology	9315	AB_490890
pTSC2 (Thr ¹⁴⁶²)	200	7	Cell Signaling Technology	3617	AB_490956
TSC2	200	2	Cell Signaling Technology	3990	AB_2209986
Vinculin	124	6	Cell Signaling Technology	13901	AB_2728768
Vinculin	124	Not recorded	Abcam	AB13007	NA
p-p44/42 (ERK1/2) (Thr ^{204/202})	42, 44	12	Cell Signaling Technology	9101	AB_331646
ERK1/2	42, 44	21	Cell Signaling Technology	4695	AB_390779

4EBP	15-20	10	Cell Signaling Technology	9452	AB_331692
p-S6 (Ser ^{240/244})	32	7	Cell Signaling Technology	5364	AB_10694233
p-S6 (Ser ^{235/236})	32	Not recorded	Cell Signaling Technology	4858	AB_916156
S6	32	9	Cell Signaling Technology	2217	AB_331355
p-p38 MAPK (Thr ¹⁸⁰ /Tyr ¹⁸²)	43	10	Cell Signaling Technology	4511	AB_2139682
p38 MAPK	40	9	Cell Signaling Technology	8690	AB_10999090
p-cJun (Ser ⁷³)	48	5	Cell Signaling Technology	3270	AB_2895041
cJun	48	13	Cell Signaling Technology	9165	AB_2130165

1496

1497 **Table S6: Secondary Antibodies**

2° Antibody	Vendor	Lot #	Cat. #	Dilution	RRID
IRDye 800CW Goat anti-Rabbit IgG (H + L)	LI-COR	D00825-14	926-32211	1:20,000	AB_621843
IRDye® 680LT Goat anti-Mouse IgG (H + L), 0.5 mg	LI-COR	D01014-04	926-68070	1:20,000	AB_10956588
Anti-rabbit IgG, HRP- linked	CST	Not recorded	7074	1:2000	AB_2099233
Anti-mouse IgG, HRP- linked	CST	Not recorded	7076	1:2000	AB_330924

1498

1499 **Table S7: Chemicals & Reagents**

Reagent	Source	Cat. #
RPMI-1640	Wisent Bioproducts	350000CL
DMSO	Fisher Scientific	BP231-100
Bortezomib (PS-241)	Cayman Chemical	10008822
Pevonedistat (MLN4924)	Selleckchem	S7109
JNK-IN-8	MedChemExpress	HY-13319
MK-2206	Cayman Chemical	11593
Borussertib	Selleckchem	S8839
VH032	MedChemExpress	HY-120217
AZD 5363	Cayman Chemical	15406
Triton X-100	Fisher	BP151-100
CellTox Green Cytotoxicity Assay	Promega	G8743
NucleoSpin RNA Plus	Takara	740984.50
Nitrocellulose membrane	Bio Rad	1620112
Milk	Fisher	NC9022655/190915ASC
Bovine Serum Albumin (BSA)	Goldbio	A-421-10
DC Protein Assay Reagent A	Bio Rad	500-0113
DC Protein Assay Reagent B	Bio Rad	500-0114
TBS-T	Boston Bioproducts	IBB-181-4L
TBS	Boston Bioproducts	IBB_596
SDS Running Buffer	Boston Bioproducts	BP-150
Transfer Buffer	Boston Bioproducts	BP-190
Methanol	Pharmco	33900HPLC
Fetal Bovine Serum	GeminiBio	A020003

Cell Titer Glo	Promega	G7570
Tandem Mass Tag (TMT) Reagents	Thermo Fisher Scientific	A34808
cOmplete, Mini Protease Inhibitor Cocktail	Roche	11836153001
PhosSTOP, Phosphatase Inhibitor Tablets	Roche	4906837001
BCA Protein Assay Kit	ThermoFisher	23227
Protease Inhibitor Cocktail	Roche	11836145001
Nucleospin RNA Plus Kit	Takara	740984.50
Nitrocellulose membrane	BioRad	1620112
PageRuler Plus	Fisher	PI26619
Protease Inhibitor Cocktail	Sigma-Aldrich	P8340-5ML
Triton X-100	Fisher Scientific	BP151-100
96-well TC treated plates	ThermoFisher	165305
60 mm TC treated dishes	Corning	430166
10 cm TC treated dishes	Westnet	353003
6-well treated tissue culture plates	Greiner	TCG-657160
Black-walled clear-bottom 96-well plates	Fisher	12-566-70
Mycoplasma Detection Kit	Lonza	LT07-218
15 cm TC treated dishes	Corning	08-772-24
NP40 substitute	Roche	11754599001

1500

1501 **Table S8: Cell Lines**

Reagent	Source	Cat. #
T47D	ATCC	HTB-133

MCF7	ATCC	HTB-22
MDA-MB-468	ATCC	HTB-132
MOLT4	ATCC	CRL-1582
BT-474	ATCC	HTB-20

1502

1503 **Table S9: Software & Algorithms**

Software	Source
GraphPad Prism	www.graphpad.com/
R Framework	www.R-project.org/
RStudio	https://www.rstudio.com/
Proteome Discoverer 2.2	Thermo Fisher Scientific
Adobe Illustrator	www.adobe.com/creativecloud.html
Affinity Designer	https://affinity.serif.com/en-gb/designer/
ImageStudioLite	https://www.licor.com/bio/image-studio-lite/

1504

1505